JGR Atmospheres

RESEARCH ARTICLE

10.1029/2024JD041366

A More Transparent Infrared Window

Eli J. Mlawer[1], Jeana Mascio[1], David D. Turner[2], Vivienne H. Payne[3], Connor J. Flynn[4], and Robert Pincus[5]

[1]Atmospheric and Environmental Research, Lexington, MA, USA, [2]NOAA/Global Systems Laboratory, Boulder, CO, USA, [3]Jet Propulsion Laboratory, California Institute of Technology, Pasadena, CA, USA, [4]University of Oklahoma School of Meteorology, Norman, OK, USA, [5]Lamont-Doherty Earth Observatory, Columbia University, New York, NY, USA

Key Points:

- Analysis of ground-based radiance observations indicates that the infrared window region is more transparent than had been thought.
- The derived water vapor self continuum is 10%–30% weaker than previously thought, while the foreign continuum is substantially stronger.
- The revised H_2O continuum results in a 5%–10% increase in climate feedback and a large change to the radiative budget for moist atmospheres.

Supporting Information:

Supporting Information may be found in the online version of this article.

Correspondence to:

E. J. Mlawer,
mlawer@aer.com

Citation:

Mlawer, E. J., Mascio, J., Turner, D. D., Payne, V. H., Flynn, C. J., & Pincus, R. (2024). A more transparent infrared window. *Journal of Geophysical Research: Atmospheres*, *129*, e2024JD041366. https://doi.org/10.1029/2024JD041366

Received 12 APR 2024
Accepted 22 SEP 2024

Author Contributions:

Conceptualization: Eli J. Mlawer
Data curation: Jeana Mascio
Formal analysis: Eli J. Mlawer
Funding acquisition: Eli J. Mlawer, David D. Turner
Investigation: Eli J. Mlawer, Jeana Mascio, David D. Turner, Vivienne H. Payne, Connor J. Flynn, Robert Pincus
Methodology: Eli J. Mlawer, Jeana Mascio, David D. Turner, Connor J. Flynn
Software: Jeana Mascio, David D. Turner
Validation: Eli J. Mlawer, Jeana Mascio
Visualization: Jeana Mascio
Writing – original draft: Eli J. Mlawer, David D. Turner, Connor J. Flynn

© 2024 The Author(s).
This is an open access article under the terms of the Creative Commons Attribution-NonCommercial License, which permits use, distribution and reproduction in any medium, provided the original work is properly cited and is not used for commercial purposes.

Abstract The infrared window region (780–1,250 cm^{-1}, 12.8 to 8.0 μm) is of great importance to Earth's climate due to its high transparency and thermal energy. We present here a new investigation of the transparency of this spectral region based on observations by interferometers of downwelling surface radiance at two DOE Atmospheric Radiation Measurement program sites. We focus on the dominant source of absorption in this region, the water vapor continuum, and derive updated values of spectral absorption coefficients for both the self and foreign continua. Our results show that the self continuum is too strong in the previous version of Mlawer-Tobin_Clough-Kneizys-Davies (MT_CKD) water vapor continuum model, a result that is consistent with other recent analyses, while the foreign continuum is too weak in MT_CKD. In general, the weaker self continuum derived in this study results in an overall increase in atmospheric transparency in the window, although in atmospheres with low amounts of water vapor the transparency may slightly decrease due to the increase in foreign continuum absorption. These continuum changes lead to a significant decrease in downwelling longwave flux at the surface for moist atmospheres and a modest increase in outgoing longwave radiation. The increased fraction of surface-leaving radiation that escapes to space leads to a notable increase (~5–10%) in climate feedback, implying that climate simulations that use the new infrared window continuum will show somewhat less warming than before. This study also points out the possibly important role that aerosol absorption may play in the longwave radiative budget.

Plain Language Summary The spectral region in the infrared from 780 to 1,250 cm^{-1} (12.8–8.0 μm) is referred to as a window due to its transparency; in this region, thermal radiation emitted by the surface can pass relatively unimpeded through the atmosphere, allowing Earth to cool. The limited amount of atmospheric absorption that does occur in this region is primarily due to water vapor, in particular an absorption mechanism termed the water vapor continuum. The strength of water vapor continuum absorption in the infrared window therefore has important consequences for Earth's climate. This study provides a new evaluation of water vapor continuum absorption in the infrared window from an analysis of spectrally resolved measurements of downwelling surface radiances. Our results indicate that for most atmospheres the strength of water vapor continuum absorption is less than had been previously thought due to reduced absorption related to the interactions of water vapor molecules with other water vapor molecules, that is, the water vapor self continuum. The derived water vapor continuum changes allow the Earth to cool ~5–10% better than had previously been thought, and climate simulations that use the revised infrared window continuum will show somewhat less warming than before.

1. Introduction

Atmospheric absorption in the infrared window (780–1,250 cm^{-1}, 12.8 to 8.0 μm) plays an important role in Earth's radiation budget and climate, a consequence of this spectral region's high thermal energy, relative transparency, and the properties of its most important source of absorption, the water vapor self continuum. The self continuum is a weak absorber under typical atmospheric conditions, but its strength increases quadratically with water vapor abundance, thus under moist conditions self continuum absorption can result in significant atmospheric opacity. The importance of the infrared window region and the dominance of the water vapor self continuum absorption in this region make it imperative that the properties of this absorber be known with high certainty so that atmospheric applications that depend on window absorption can be regarded with confidence. This study presents the result of a new radiative closure analysis (Mlawer & Turner, 2016; Shepherd et al., 2003) of water vapor continuum absorption in the infrared window.

Writing – review & editing: Eli J. Mlawer, Jeana Mascio, David D. Turner, Vivienne H. Payne, Connor J. Flynn, Robert Pincus

Table 1
Most of the Transparent Portion of the Longwave Region is in the Infrared Window

Reference atmosphere	Precipitable water vapor (cm)	Total surface flux (W/m^2)	Surface flux for OD < 1	Fraction of OD < 1 flux in IR window
Tropical	4.1	451.62	155.56	0.98
Midlatitude summer	2.9	420.03	171.19	0.97
US standard	1.4	387.41	199.71	0.85
Subarctic summer	2.1	382.15	158.48	0.96
Midlatitude winter	0.9	309.34	178.37	0.74
Subarctic winter	0.4	247.16	165.62	0.60

Note. For six reference atmospheres: total upwelling longwave flux at the surface, precipitable water vapor, upwelling flux in the portions of the longwave that are sufficiently transparent (vertical optical depth < 1) so that a significant fraction of the radiation emitted by the surface reaches the top of the atmosphere, and the fraction of the transparent-region surface flux that is in the infrared window region. Surface emissivity is assumed to be unity.

Longwave radiation that escapes to space (outgoing longwave radiation or OLR) is a critical component of the Earth's radiation budget. Most of the thermal radiation emitted by the Earth's surface is absorbed by the atmosphere, which then emits thermal radiation at its own temperature, which typically is less than the surface temperature. An exception to this general behavior occurs in spectral regions that are relatively transparent in clear skies, in which the warm radiation emitted by the surface is only slightly attenuated and therefore escapes the atmosphere. These spectral regions are called "windows"—the most important with respect to Earth's thermal radiation is the infrared window. For six reference atmospheres, Table 1 shows the total surface flux emitted by the surface, the surface flux in spectral regions in which the total vertical optical depth is less than 1, and the fraction of this "transparent-region" flux that is in the infrared window. These values indicate that only a limited amount of the surface flux has the potential to escape to space, and a large fraction of that amount is in the infrared window.

The infrared window plays a crucial role in climate and climate feedback (e.g., Jeevanjee et al., 2021; Koll & Cronin, 2018; Seeley & Jeevanjee, 2021). At typical current surface temperatures the infrared window is the primary spectral region in which the radiation that escapes to space can change as the planet adjusts to an energy imbalance, such as is being currently precipitated by anthropogenic increases in greenhouse gases. The infrared window is also critically important with respect to downwelling and net flux at the surface. In opaque spectral regions, the downwelling flux arriving at the surface typically is emitted at a temperature close to the surface temperature, resulting in a small net flux at the surface. In contrast, in the infrared window emitted downwelling radiation that reaches the surface is usually significantly smaller than the upwelling radiation, leading to a large net flux. The net flux divergence, which drives radiative cooling and heating, is also of unique importance in this window. The quadratic dependence on water vapor abundance of the self continuum optical depths leads to large relative gradients in optical depth in the lower atmosphere, and therefore large radiative flux divergences. Due to this effect, for moist atmospheres around 75% of the longwave cooling rate near the surface occurs in the window (Mlawer et al., 1997).

Section 2 of this paper provides background information on water vapor continuum absorption in the infrared window. Section 3 presents information about the radiometric measurements used in this study, the radiative transfer model calculations used to compare with these measurements, and details about how the atmospheric properties used in the calculations were obtained. Section 4 contains details about how the measurement-calculation differences were analyzed and then utilized to derive self and foreign continuum coefficients in the infrared window, as well as the temperature dependence of the self continuum. Section 5 compares the derived results to results obtained in previous studies and Section 6 discusses the impact of the new window water vapor continuum results on atmospheric applications. Section 7 provides a summary and discussion.

2. The Water Vapor Continuum in the Infrared Window

In this study, we consider the Mlawer-Tobin_Clough-Kneizys-Davies (MT_CKD) water vapor continuum model (Mlawer et al., 2012, 2023), the primary source used in the community to specify water vapor continuum absorption in the thermal infrared spectral region. We provide a summary here of important points concerning the

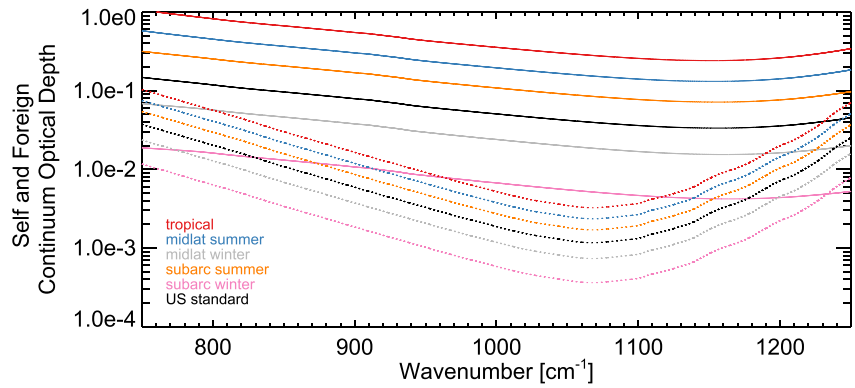

Figure 1. Optical depths due to the MT_CKD_4.1.1 water vapor self (solid) and foreign (dotted) continua for a vertical path for six reference atmospheric profiles.

evolution of the MT_CKD model and relevant laboratory measurements in the atmospheric window. Water vapor continuum parameters discussed in this section are defined in Mlawer et al. (2023) and for convenience are provided below in Section 3.2.

For reference, self and foreign continuum optical depths from the current version of MT_CKD (v4.1.1) are shown in Figure 1 for six reference profiles. Figure 2c indicates that the most recent laboratory measurement of the self continuum in this region (Baranov et al., 2008) agrees well at atmospheric temperatures with the MT_CKD continuum model, which is based on a field study (Turner et al., 2004), despite a disagreement in the temperature dependence (Figure 3). (Further details and historical perspective can be found in Section S1 in Supporting Information S1.) However, a direct comparison between self continuum coefficients from laboratory measurements and field studies does not provide a full picture.

There is an important distinction between the window self continuum values based on field studies (i.e., those that motivated the development of CKD_2.1 and MT_CKD_1.0, as shown in Figure 2b) and those based on laboratory studies (Figure 2c). Laboratory studies utilize cells that contain pure water vapor, while the atmospheric paths relevant to field studies are comprised of mostly air (primarily nitrogen and oxygen) with a small fraction of water vapor. Therefore, field studies of the self continuum have a dependence on the water vapor foreign continuum, while laboratory studies typically do not. Although the foreign continuum is much weaker than the self continuum in the window (Figure 1), significantly inaccurate values assumed for the foreign continuum can still have an impact on the derived self continuum in analyses of field observations. Therefore, the evolution of window foreign continuum values is key to a proper understanding of past field studies of window self continuum absorption.

The original CKD foreign continuum values (Clough et al., 1989) in the window were based on Burch (1982), which supported the conclusion that the foreign continuum was a very weak absorber in this region (Figure 4). A major increase in the window foreign continuum came about with advent of MT_CKD (Mlawer et al., 2012), which resulted not from new foreign continuum measurements in this region but rather as a consequence of constraining the model's derived line shape parameters to fit the foreign continuum behavior from 500 to 750 cm^{-1} in its predecessor version, CKD_v2.4.1. These increased MT_CKD foreign continuum coefficients in the window were subsequently shown to be consistent with field observations by Turner et al. (2004). Even with this increase, foreign continuum absorption in this region remained rather weak compared to that of the self continuum. However, more recent laboratory measurements (Baranov & Lafferty, 2012; Cormier et al., 2005) supported a much higher level of foreign continuum absorption. As can be seen in Figure 4, the Baranov and Lafferty (2012) study indicated that the foreign continuum was ~2–4 times greater than MT_CKD_1.0, although the reported strength was about half as large as specified in Cormier et al. (2005). Given the relative optical depths of the window foreign and self continua shown in Figure 1, assuming a 2–4 times larger foreign continuum would have an appreciable effect on the self continuum absorption derived in a field study.

It is instructive to understand to what extent the self continuum values derived in previous field studies would have been affected had a stronger foreign continuum been utilized in these studies instead. To evaluate this, we modify the current version of MT_CKD (v4.1.1) such that the window foreign continuum coefficients are increased to be generally consistent with the Baranov and Lafferty (2012) values. This modified foreign

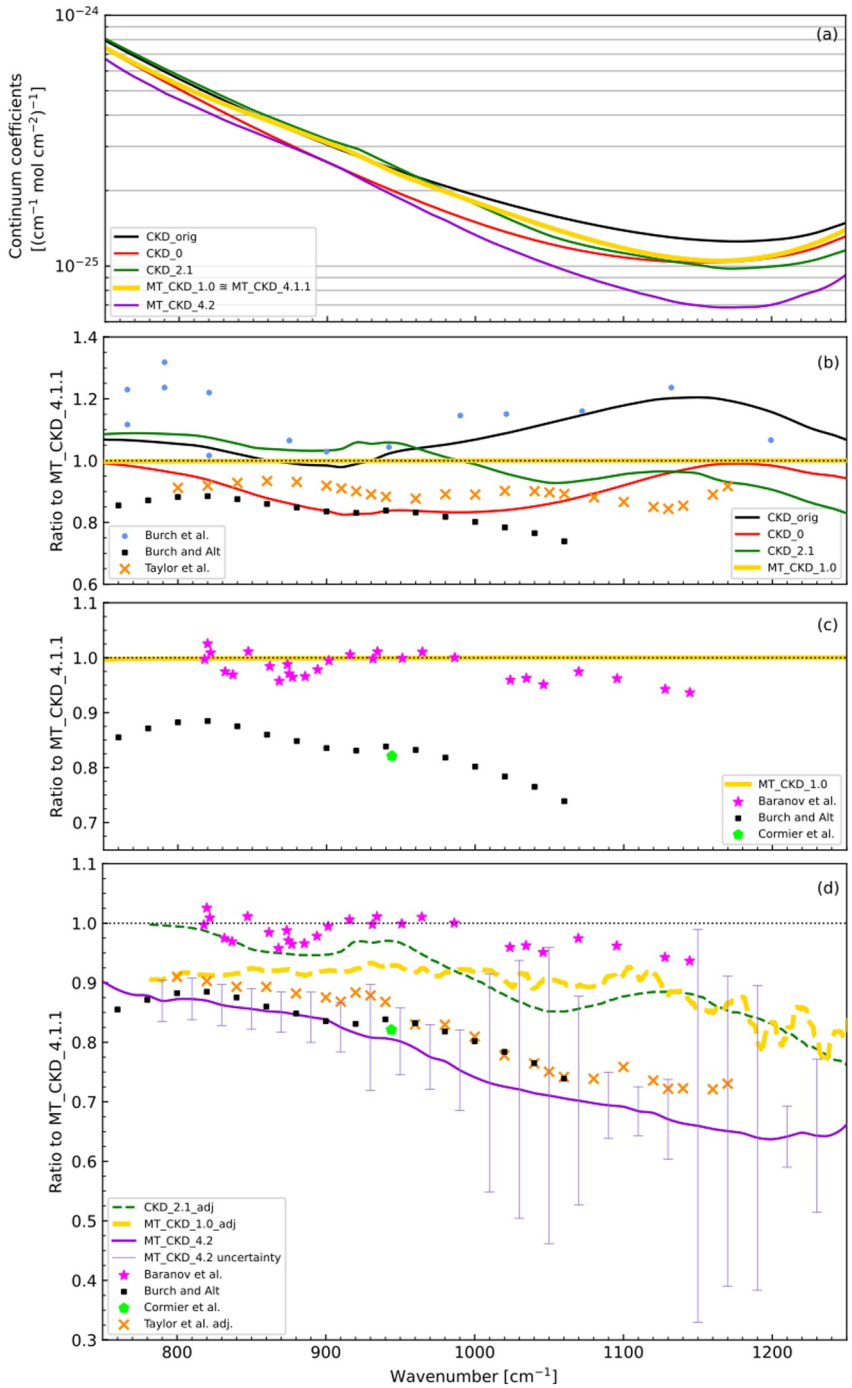

Figure 2. Various perspectives on the water vapor self continuum in the infrared window. (a) Water vapor self continuum coefficients for five versions of the CKD and MT_CKD continuum. The yellow curve is the self continuum at the beginning of this study, MT_CKD_4.1.1, and the purple curve shows the result of this study, MT_CKD_4.2; (b) Overview of the self continuum in ~2004. Shown as ratios with respect to MT_CKD_4.1.1 are several previous versions of CKD and MT_CKD as well as two sets of laboratory measurements (blue circles and black squares) and the result from the Taylor et al. (2003) field campaign (orange X's); (c) Key evaluations of the self continuum before this study are shown as ratios with respect to MT_CKD_4.1.1; (d) Overview of the self continuum after this study. Shown as ratios with respect to MT_CKD_4.1.1 are the most recent laboratory measurements from three groups (pink stars, black squares, and green pentagon) and the results from three field studies (Taylor et al., 2003, orange X's; CKD_2.1 (green dashed curve), which was motivated by Westwater et al., 1995); MT_CKD_1.0 (yellow dashed curve), which was motivated by Turner et al. (2004) that have been adjusted to account for a stronger foreign continuum (as described in Section 2) than had been used in their respective original analyses. The purple curve shows the significant decrease in the self continuum that is derived in this study, MT_CKD_4.2—note that in some regions the corresponding derived error (purple vertical lines with end caps) is significant.

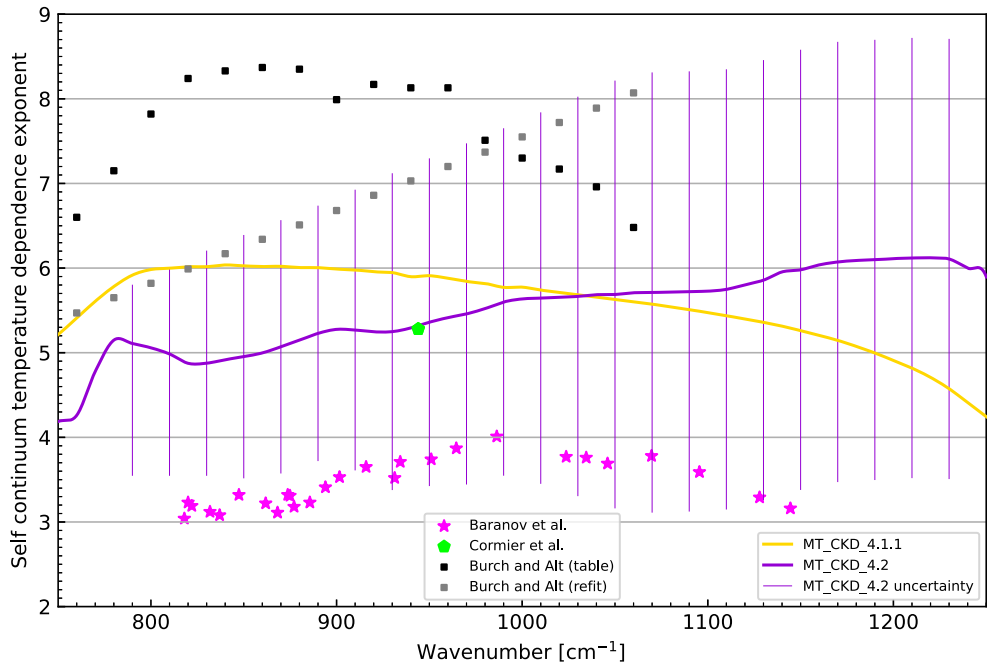

Figure 3. The temperature exponent n (see Equation 5) of the self continuum coefficients from 750 to 1,250 cm^{-1} from several laboratory studies (various symbols), the previous version of MT_CKD, v4.1.1 ≅ v1.0 (yellow curve), and the version derived in this study, MT_CKD_4.2 (purple curve), with estimated uncertainties shown in vertical purple lines without end caps.

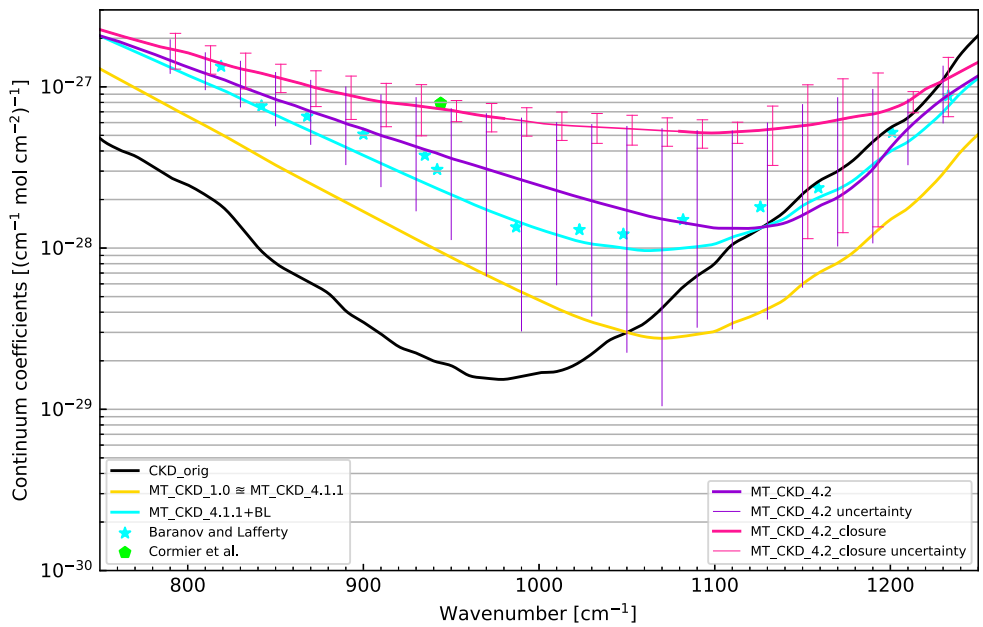

Figure 4. Water vapor foreign continuum coefficients from 750 to 1,250 cm^{-1} for the original version of the CKD model (black curve), the current version of the MT_CKD model (v4.1.1, which is equivalent to MT_CKD_1.0, yellow curve), the laboratory results from Baranov and Lafferty (2012, cyan stars) and Cormier et al. (2005, green pentagon), and a version of MT_CKD (v4.1.1+BL, cyan curve) that was adjusted to be consistent with the Baranov and Lafferty (2012) results. The foreign continuum derived in this study, MT_CKD_4.2, is shown in purple, with associated uncertainty values shown with vertical lines without end caps. The pink curve shows the foreign continuum (MT_CKD_4.2_closure) needed to obtain radiative closure with the Southern Great Plains (SGP) observations used in this study. Error bars based on the SGP data set are pink vertical lines (slightly offset in the x-direction for clarity) with end caps.

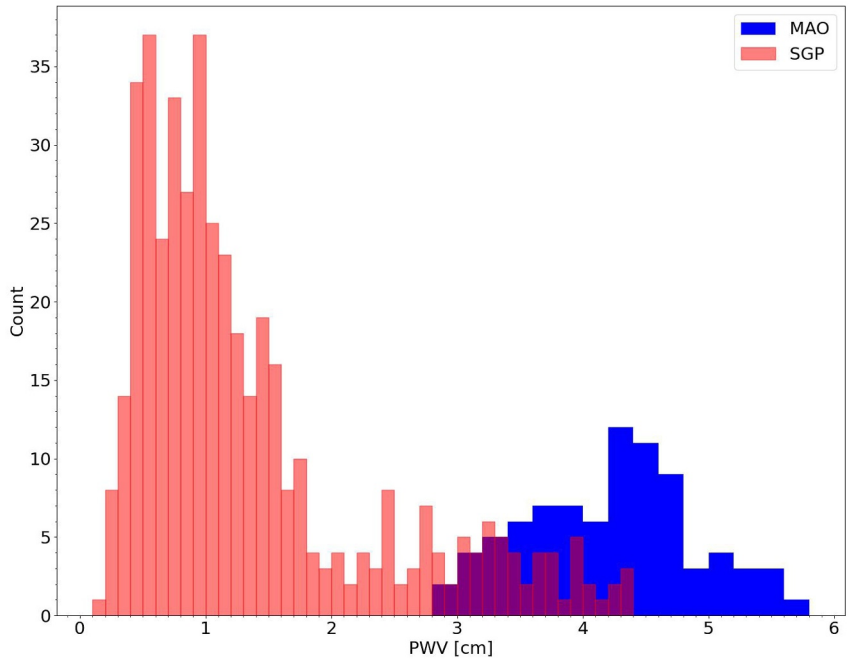

Figure 5. Precipitable water vapor amounts for the cases used in this study.

continuum version is shown as MT_CKD_4.1.1+BL in Figure 4. We use this modified version to estimate (method described in Appendix A) the change in the self continuum values that would have been obtained in three prior field studies had a greater foreign continuum been assumed rather than the values that actually were used in these studies. These reconsidered self continuum values are shown in Figure 2d as MT_CKD_1.0_adj, CKD_2.1_adj, and Taylor_adj (which, respectively, are based off the studies of Turner et al. (2004), Westwater et al. (1995)/Han et al. (1997), and Taylor et al. (2003)). We also include on this figure the self continuum laboratory results of Cormier et al. (2005), Baranov et al. (2008), and Burch and Alt (1984), which improved upon the previous measurements by the Burch group.

The overall impression given by Figure 2d is murkier than in Figure 2c (or in Figure 8 of Baranov et al., 2008), but the observational evidence clearly allows the possibility that the window self continuum is significantly weaker than in current MT_CKD. However, the diversity of values shown suggests that there is no consensus for the strength of the window self continuum. The main motivation for this current study is to bring some clarity to this question of great importance.

3. Elements of the Comparison

Our analysis of water vapor continuum absorption in the infrared window is based on comparisons between clear-sky radiance measurements by the Atmospheric Emitted Radiance Interferometer (AERI; Knuteson et al., 2004a, 2004b) and corresponding calculations by the Line-By-Line Radiative Transfer Model (LBLRTM; Clough et al., 2005). The LBLRTM calculations use as input a combination of in situ measurements, retrieved quantities, and model output.

Our radiative closure analysis is based on observations taken at two sites operated by the DOE Atmospheric Radiation Measurement (ARM) program. The primary data set is more than 2 years of observations (March 2016–October 2018) from the ARM Southern Great Plains (SGP) site, the world's largest and most extensive climate research facility. The SGP site consists of in situ and remote-sensing instrument clusters and has been collecting data since it was established in 1993. Also used in this study are observations from the ARM Observations and Modeling of the Green Ocean Amazon (GoAmazon; Martin et al., 2016) campaign (MAO), held from January 2014 through October 2015 in Manaus, Brazil. Due to MAO's tropical location the median precipitable water vapor (PWV) amount for the profiles used in our analysis is far greater than for SGP (Figure 5) and provide an excellent data set for validating the self and foreign continuum derived from SGP observations.

We provide here details about each of the three elements (measured radiances, modeled radiances, and specification of the atmospheric state) involved in this radiative closure study.

3.1. Radiometric Measurements

Measurements from the AERI, a Fourier transform infrared interferometer that measures downwelling spectrally resolved infrared radiance from 550 to 3,000 cm^{-1} (Turner et al., 2016), are used in this study. An AERI uses two detectors to have sensitivity to radiance in the 3.3–19 μm band, and the maximum optical path delay provides a spectral resolution of 0.5 cm^{-1}. The instrument regularly views two well-characterized blackbodies, which are operated at ambient temperature and 60°C, respectively. These blackbody observations, together with a correction for the detector's non-linearity, allows the instrument to measure downwelling spectral infrared radiance with a radiometric accuracy better than 1% of the ambient radiance. Additionally, a calibrated metrology laser and corrections for the finite field-of-view of the instrument provide spectral calibration. Details on the instrument and its calibration method are provided in Knuteson et al. (2004a, 2004b).

The signal observed from the sky is calibrated using the ambient and hot blackbody views using the complex arithmetic technique proposed by Revercomb et al. (1988). However, careful analysis has shown that there can still exist a slight positive bias to the observed sky radiance; this is most easily seen in extremely dry clear-sky scenes (Delamere et al., 2010; Turner, 2003). Initially, the source of this bias was assumed to be something in the foreoptics (e.g., a small amount of scattered ambient radiation). More recently, a new hypothesis was formulated suggesting that emission from the aft optics is not accounted for in the calibration. The functional form of an aft optics correction would be the same as used in Delamere et al. (2010), with the contribution from the "offending" temperature being that of the aft optics. However, Delamere et al. (2010) and earlier studies used data from version 2 AERIs (see the appendix in Turner et al., 2016), while the AERIs used in this study are considered version 4 and have small changes to the optics of the instruments relative to version 2. For this study, the observations did not definitively support either an issue with the foreoptics or the aft optics, thus no bias correction was applied.

A zenith-looking AERI, deployed at an altitude of 320 m, has been providing operational radiance measurements at SGP since 1995, observing radiances emitted downward by the atmosphere for a large range of water vapor column amounts. Similarly, an AERI was deployed (altitude of 50 m) at MAO during GoAmazon. Figure 6 shows average AERI radiances from observations used in this study for different PWV ranges.

3.2. Model Calculations

Radiance calculations by LBLRTM_v12.15.1 are used in our radiative closure analysis, which focuses on the 780–1,280 cm^{-1} region. Absorption line parameters used in these calculations utilize the line file version AER_v3.8.1 and continuum absorption is specified by MT_CKD_4.1.1 (for our baseline calculations). (These models and databases are available at https://github.com/AER-RC, the GitHub repository of the AER Radiation and Climate Group.) We also perform LBLRTM calculations for which the water vapor continuum is changed to MT_CKD_4.1.1+BL. All calculations used in this study include all relevant absorption due to water vapor, carbon dioxide (including first-order line coupling), ozone, nitrous oxide, methane (first-order line coupling), ammonia, CCl4, CFC-11, CFC-12, HNO_3, HCFC-22, and PAN.

The MT_CKD water vapor continuum model (Mlawer et al., 2012, 2023) provides water vapor self and foreign continuum coefficients (cm^2/molecule/cm^{-1}) every 10 cm^{-1} from 0 to 20,000 cm^{-1}. To obtain continuum coefficients in between the stored values, a cubic interpolation using the four closest stored values is performed. Absorption coefficients C_x (cm^2/molecule) can be obtained by multiplying the continuum coefficients $\tilde{C}_x$ by the radiation term R as follows:

$$C_x(\nu,T,\rho_x) = \tilde{C}_x(\nu,T,\rho_x)\, R(\nu,T) \tag{1}$$

where ν is the wavenumber, T is the temperature, the subscript "x" denotes either "self" or "foreign," and the radiation term R is given by the following equation:

$$R(\nu,T) = \nu \tanh\left(\frac{hc\nu}{2kT}\right), \tag{2}$$

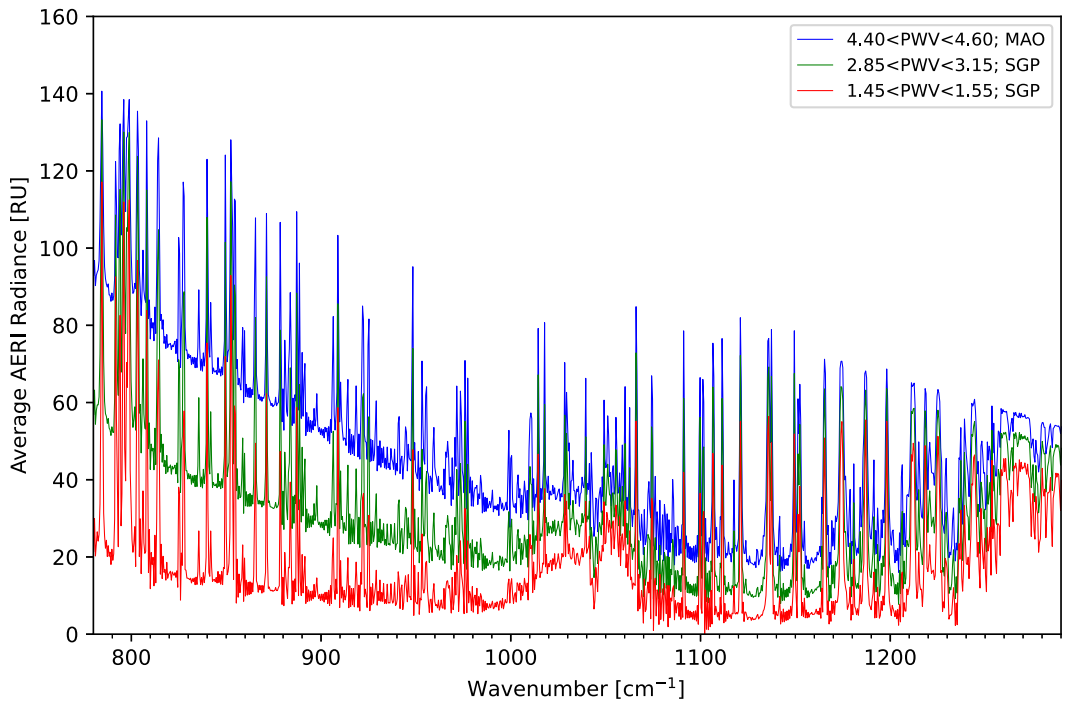

Figure 6. Average AERI radiances used in this study from MAO (blue curve) and for two precipitable water vapor bins at Southern Great Plains (red and green curves). A "radiance unit" (RU) is 1 mW/(m^2 sr cm^{-1}).

where h is Planck's constant, c is the speed of light, and k is Boltzmann's constant. The dependence on density implied by the notation for $\tilde{C}_x$ is given by the following equation:

$$\tilde{C}_x(\nu,T,\rho_x) = \tilde{C}_x(\nu,T,\rho_{x,ref})\left(\frac{\rho_x}{\rho_{x,ref}}\right) \tag{3}$$

where ρ is the density of the gaseous molecules interacting with water vapor in the respective process (i.e., water vapor for the self continuum; all gaseous molecules except for water vapor for the foreign continuum) and the reference density at which coefficients are stored corresponds to a pressure of 1,013 mbar and a temperature of 296K. The optical depth of the self or foreign continuum is given by the product of the absorption coefficient C_x and the water vapor column amount W (molecules/cm^2) as follows:

$$\tau_x(\nu,T,\rho_x) = W(H_2O)\, C(\nu,T,\rho_x). \tag{4}$$

The temperature dependence of the self continuum coefficients in the MT_CKD model is given by the following equation:

$$\tilde{C}_s(\nu,T) = \tilde{C}_s(\nu,296K)\,(296/T)^{n(\nu)} \tag{5}$$

where n is a wavenumber-dependent dimensionless parameter and the density dependence of the coefficients has been suppressed for clarity. The foreign continuum coefficients are assumed not to be dependent on temperature.

More details about this formulation can be found in Mlawer et al. (2023).

3.3. Specification of the Atmospheric State

Multiple observations are used to create the profiles used as input to the model calculations. The foundation for the temperature and water vapor profiles are observations by radiosondes (hereafter sondes), which were usually launched four times daily during our study period at SGP and twice a day at MAO. However, sonde measurements

are not directly used as input to the radiative transfer calculations in our analysis. The sonde launch location at SGP is ~250 m from where the AERI is deployed so its measured temperatures and humidity values in the lowest several hundred meters cannot provide the required accuracy for our closure study, and sonde humidity measurements have well-known accuracy issues (Turner et al., 2016). For our study, we use the TROPoe (Turner & Löhnert, 2014) physical retrieval algorithm to retrieve profiles of temperature and humidity that provide closure with the sonde profiles, the AERI radiance observations between 538 and 722 cm^{-1} (i.e., regions of the spectrum wherein the water vapor line shape and continuum absorption have undergone validation (Delamere et al., 2010; Mlawer et al., 2019)), and the brightness temperatures at 23.8 and 31.4 GHz from a microwave radiometer (MWR; Cadeddu et al., 2013). For this study, the TROPoe retrieval utilizes the latest version of the MT_CKD continuum (v4.1.1; Mlawer et al., 2023) and the AER line file, ensuring that its water vapor spectroscopy from 538 to 722 cm^{-1} includes recent upgrades.

The TROPoe algorithm is a 1-dimensional variational retrieval approach using the optimal estimation framework. It has been extensively modified to include a wide number of measurements (with their uncertainties) from different instruments in the observation vector (Turner & Blumberg, 2019; Turner & Löhnert, 2021). A prior data set is used to constrain the retrieval; for SGP, sonde launches from over 10 years were used to create seasonal priors, whereas all the sondes launched during the Go-Amazon field campaign were used to create the single yearly prior for the MAO site. Ultimately, the retrieval finds the solution (i.e., the retrieved thermodynamic profiles) that provides the best fit with all the observations (i.e., sonde, AERI radiances, and MWR brightness temperatures) and the prior (within their uncertainties). The TROPoe retrieval is run at the sonde launch time.

The TROPoe profiles only extend to 17 km, as that is the maximum height of the prior data set used to constrain the retrieval. Above 17 km, temperature values from Modern-Era Retrospective analysis for Research and Applications, Version 2 (MERRA-2; Randles et al., 2017) are used. For water vapor, values are taken from reference atmospheric profiles (U.S. standard for SGP, tropical for MAO) (Anderson et al., 1986) above 17 km. For the SGP cases used in this study, the ratios of the PWV values of the TROPoe-derived and sonde profiles average 0.984 (stdev 0.015) with virtually no dependence on PWV.

In the uncertainty analysis of the water vapor continuum absorption parameters derived in this study (Section 4.6), an alternative data set of temperature and water vapor profiles is also considered. This specification directly uses the sonde-measured temperature and water vapor profiles in which the sonde water vapor measurements are scaled such that agreement is attained between the 23.8 GHz measurement of the collocated MWR and a corresponding radiative transfer calculation (Turner et al., 2016). This method to specify the thermodynamic profile has been previously used in similar radiative closure studies (e.g., Mlawer & Turner, 2016; Turner et al., 2004). For the SGP cases used in this study, the ratios of the PWV values of the TROPoe-derived and MWR-scaled sonde profiles average 0.988 (stdev 0.011).

The profiles of trace gas abundances that are used in the radiative transfer calculations are obtained from multiple sources. MERRA-2 profiles corresponding to the SGP and MAO locations are used to specify ozone. For CO_2, N_2O, CH_4, HCOOH, HNO_3, and PAN, monthly climatologies for each year are used; these were originally developed for the NASA Aura satellite project and updated over time by the Tropospheric Emission Spectrometer (TES; Worden et al., 2007) and TRopospheric Ozone and its Precursors from Earth System Sounding (TROPESS; Worden et al., 2022) teams. Monthly climatologies from TES/TROPESS are also used for four other molecules (CCl_4, CFC-11, CFC-12, and HCFC-22), which are scaled to be consistent with surface abundance values from the NOAA Halocarbons and other Atmospheric Trace Species (HATS) program (https://gml.noaa.gov/hats/flask/flasks.html). All other molecular profiles are specified using the reference values stored in LBLRTM (U.S. standard atmosphere for SGP, tropical atmosphere for MAO).

4. Results of Measurement-Calculation Comparisons

4.1. Case and Channel Selection

More than 3,000 sondes were launched at SGP during our study period. For each sonde, AERI measurements (~90) within a 35-min window associated with each sonde launch ($t - 5$ to $t + 30$ min) are averaged. Given the large number of sondes and the many AERI channels in the targeted spectral region (780–1,280 cm^{-1}), we can be selective with respect to the AERI radiance measurements we use in the study to minimize the possibility that our analysis is affected by clouds, insensitivity to water vapor continuum absorption, and trace gas uncertainty.

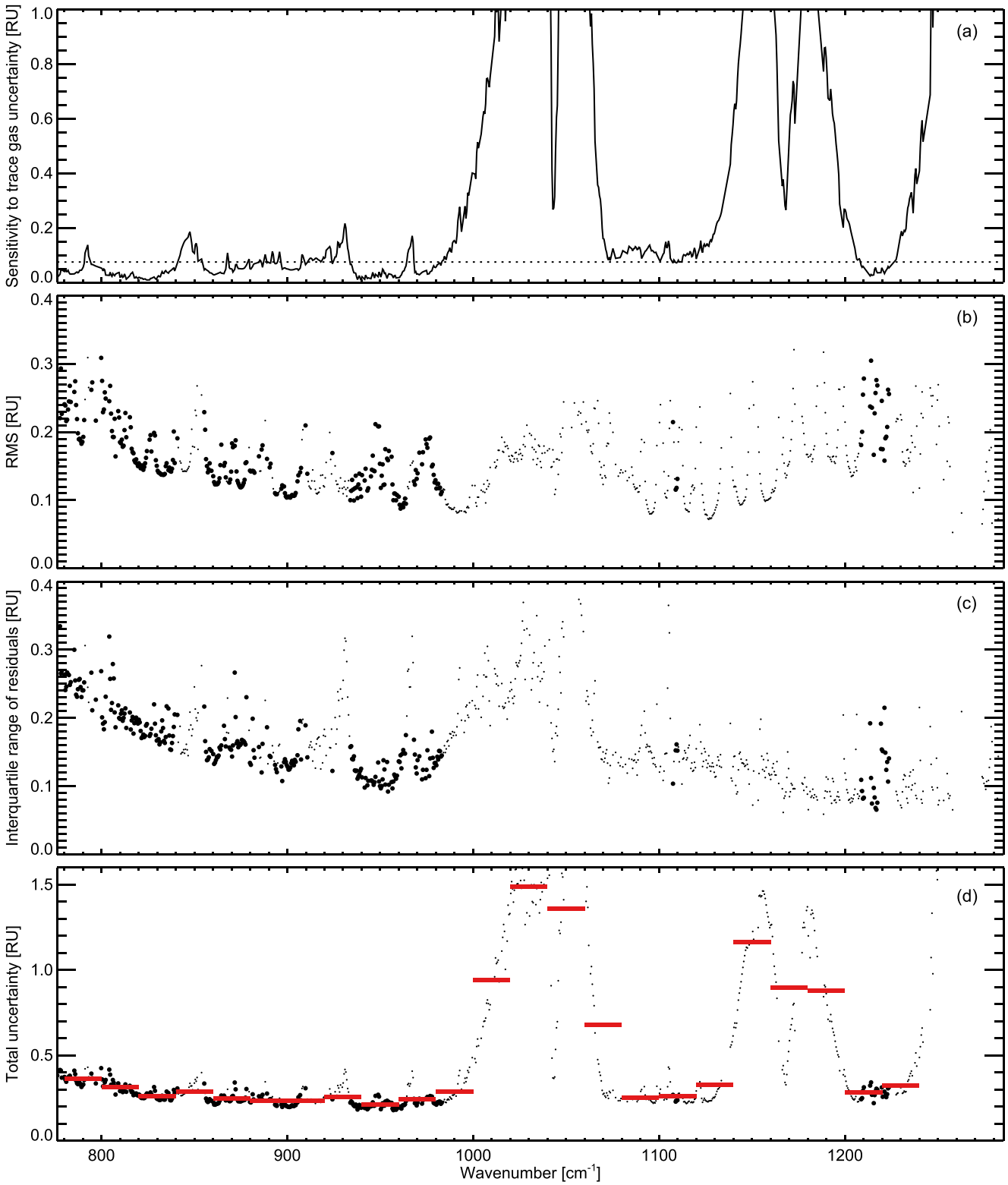
Sensitivity to trace gas uncertainty [RU]
(a)
RMS [RU]
(b)
Interquartile range of residuals [RU]
(c)
Total uncertainty [RU]
(d)
Wavenumber [cm-1]

Figure 7.

To avoid cloud contamination, we remove cases where a cloud might be contributing to the downwelling infrared radiance using two tests: the cloud liquid water path retrieved by TROPoe is less than 2 g/m^2 and the magnitude of the standard deviation of the 900 cm^{-1} radiance observation over the 35-min window is less than 0.3 RU. This initial screening removes cases that fail either of these tests for the presence of clouds, resulting in 453 cases being identified as clear-sky observations.

Our analysis of the water vapor continuum focuses on AERI channel measurements that are sensitive to the strength of water vapor continuum absorption. These spectral elements are identified by evaluating the sensitivities of all AERI channels to a change in continuum strength. We first compute the change in spectral radiances for all clear AERI cases due to a small perturbation in the self continuum, then bin these sensitivity values into 10 cm^{-1} spectral bins and five PWV ranges. For each spectral bin and PWV range, we classify each channel in all AERI cases as either "sensitive" or "insensitive" by computing a threshold between the two classes based on minimizing the combined variance in both classes (Otsu, 1979). AERI channels that are classified as "sensitive" for at least 50% of the cases in at least three of the five PWV ranges are used in the SGP analysis, and the other channels are not considered further in our retrieval of water vapor continuum coefficients.

Given the very low optical depths associated with the foreign continuum (Figure 1), a small error in the specification of trace gas abundances can impact the determination of foreign continuum coefficients from the AERI measurements. This can then impact the accuracy of the derived self continuum. To identify AERI channels that may be non-trivially impacted by inaccurate specification of trace gas abundances, the uncertainty for each abundance value is required. We use a conservative estimate of ~2 ppm for CO_2, while the uncertainty in the total column amount of N_2O is estimated as 1% and CH4 as 0.02 ppmv. For HNO_3 and PAN, the uncertainty is calculated as the standard deviation of the monthly values for this location in the climatologies. For NH_3 and HCOOH, we use estimated uncertainties of 50%. For ozone, following Wargan et al. (2017), the stratospheric and tropospheric uncertainties are estimated as 8% and 21%, respectively. For CCl_4, CFC-11, CFC-12, and HCFC-22, the uncertainty is set to be consistent with the variance of the respective source value in the HATS database. Using the uncertainty values for all trace gases, a sensitivity study is performed corresponding to an AERI observation associated with a moderate PWV value (2.15 cm) and spectral differences are computed between a baseline calculation in which the trace gases are at their standard abundances and a perturbed calculation in which these abundances are increased by their respective uncertainties. The results from these calculations are shown in Figure 7a. For a chosen uncertainty threshold value of 0.075 RU, we consider water vapor continuum coefficients derived at spectral points for which the sensitivity to trace gas abundances exceeds this threshold to be less reliable, while those AERI channels below this threshold and thus showing less sensitivity to trace gas uncertainty are considered more reliable. Certain figures in this paper (Figures 7 and 9–11) distinguish between these two categories of AERI channels through the use of large circles (greater confidence) and small circles (lesser confidence). (The uncertainty threshold is significantly exceeded throughout the ozone band from 980 to 1,080 cm^{-1} and radiative closure results in this spectral region are not presented in this study to avoid confusion.)

4.2. Initial Analysis

For each selected AERI channel, the residuals (measurement minus calculation) between the AERI radiance measurements and corresponding LBLRTM calculations are grouped into 0.1 cm PWV bins. We eliminate the impact of possible outliers by only considering the results in a PWV bin for cases that have a residual between the 25th and 75th quartiles. The mean of this "inner half" of cases is computed for all PWV bins (for each set of LBLRTM calculations considered in this study).

For illustration, the behavior of these binned mean residuals as a function of PWV is shown in Figure 8 for three AERI channels. Results are shown for LBLRTM calculations that use MT_CKD_4.1.1 (black) and MT_CKD_4.1.1+BL (green; description in Section 2). The dependence of the residuals on PWV, fit with a quadratic function for each channel, indicates that the measurement data set is not consistent with the LBLRTM

Figure 7. For AERI channels from 780 to 1,280 cm^{-1}: (a) Difference in calculated radiances due to the changes to abundances of trace gases described in Section 4.1. The analysis in this study at spectral locations for which this change is less than the horizontal dotted line are viewed with greater confidence; (b) RMS differences between radiances calculated with profiles utilized in this study and reasonable alternate profiles (as described in Section 4.6); (c) Interquartile range of measurement-calculation differences for all precipitable water vapor bins; (d) Total spectral uncertainty of measurement-calculation residuals (black circles) and RMS of uncertainties in 20 cm^{-1} regions (red horizontal lines).

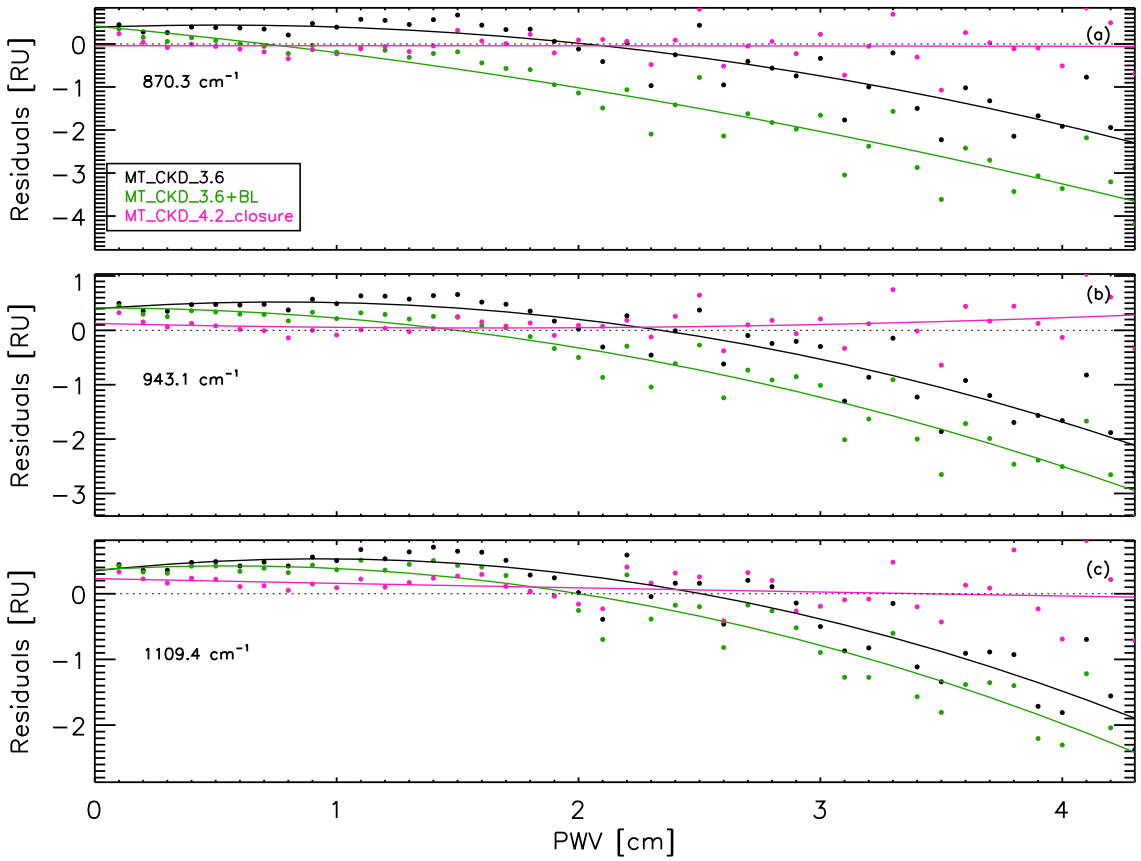

Figure 8. Residuals between AERI measurements at Southern Great Plains and corresponding LBLRTM calculations as a function of precipitable water vapor (PWV) for three AERI channels in the infrared window. The black symbols are for LBLRTM calculations that use MT_CKD_4.1.1, the green symbols correspond to the use of MT_CKD_4.1.1+BL, and the pink symbols result from using the continuum derived in this study, MT_CKD_4.2_closure. Quadratic fits to these residuals are shown as curves in corresponding colors. Cases are binned by PWV and analyzed as described in Section 4.3.

calculations for either of these specifications of self and foreign water vapor continuum absorption. Furthermore, the behavior of the residuals as a function of PWV suggests that more atmospheric opacity is needed in the calculation for low PWV amounts, while the opacity is overestimated for higher PWV values. Other channels in the infrared window show similar results.

The medians (over PWV bins) of the inner-half mean residuals for calculation using MT_CKD_4.1.1 (black) and MT_CKD_4.1.1+BL (green) are shown in Figure 9a for each AERI channel analyzed. Although MT_CKD_4.1.1 appears to provide reasonable results, the results in this panel are misleading. As for the three channels shown in Figure 8, a quadratic curve is fit to the values of binned mean residuals versus PWV for all AERI channels. The linear and quadratic coefficients of the fit for each channel are shown in Figures 9b and 9c, respectively. Reasonable overall agreement between the measured and calculated radiances would result in residuals that would have little dependence on PWV—the values in Figures 9b and 9c would be more-or-less zero (i.e., follow each panel's *x*-axis). This is not the case for either version of LBLRTM (4.1.1 and v4.1.1+BL) available prior to this study.

Since the foreign continuum depends linearly and the self continuum quadratically on the water vapor amount, there is some validity in associating the behavior of the linear fit coefficient, as shown in Figure 9b, with an inaccurate specification of the foreign continuum and the behavior of the quadratic coefficient (Figure 9c) with the self continuum. However, due to the dependence of each on pressure, and hence on the water vapor profile and not simply on PWV, and the dependence of the self continuum coefficients on temperature, such an association is not exact. A modification in the specification of either continuum source will lead to changes in both the linear and quadratic fit coefficients, so improvements to the results shown in Figure 9 can follow only from a simultaneous analysis of the foreign and self continua.

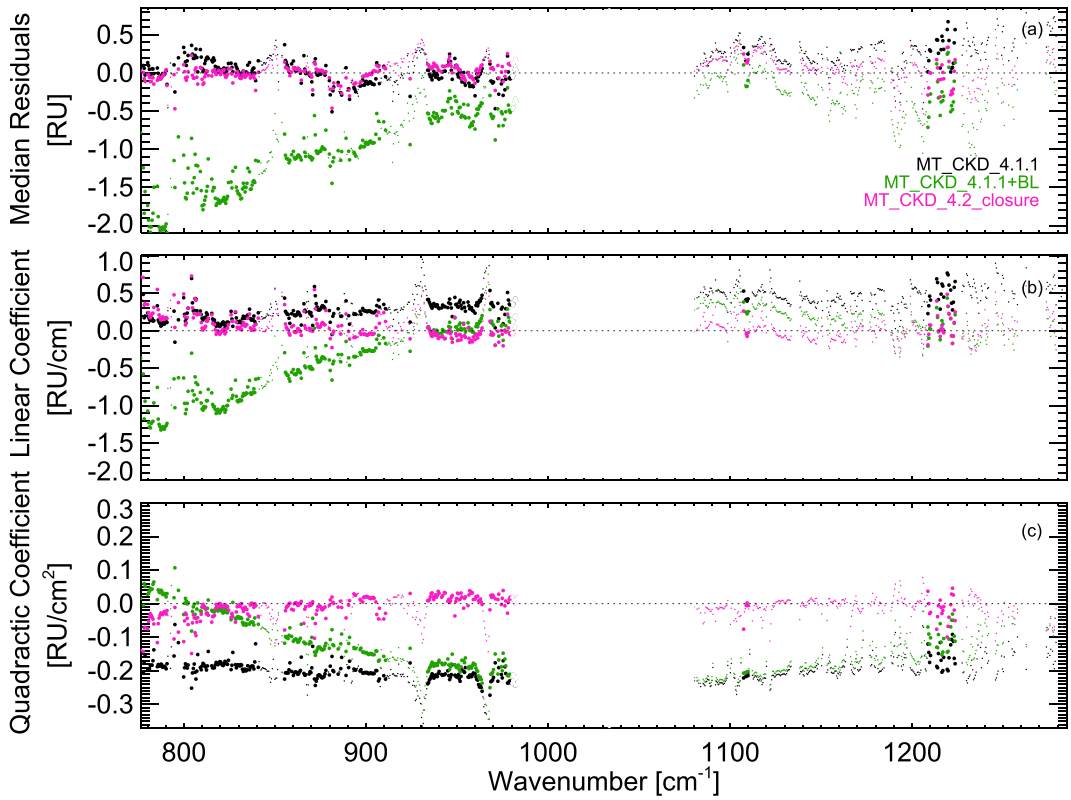

Figure 9. Comparison between AERI measurements at Southern Great Plains and corresponding LBLRTM calculations for the spectral region 780–1,280 cm^{-1}: (upper) Median of the PWV-binned residuals. The residual for each spectral point in a precipitable water vapor (PWV) bin is computed as the mean of the "inner half" of all residuals in that bin, as described in Section 4.2. The black symbols are for LBLRTM calculations that use MT_CKD_4.1.1, the green symbols correspond to MT_CKD_4.1.1+BL, and the pink symbols result from using the continuum derived in this study, MT_CKD_4.2_closure; (middle) Linear coefficient of the quadratic fit to the residuals as a function of PWV; (bottom) Quadratic coefficient of the quadratic fit to the residuals as a function of PWV. The distinction between large and small circles is explained in Section 4.1.

4.3. Retrieval of Self and Foreign Continua

Our SGP AERI data set, with its large number of cases and wide range of PWV values, is ideal for retrieving self and foreign continuum coefficients in the infrared window. The wide range of temperatures that characterize the water vapor profiles associated with these AERI observations also may allow the derivation of coefficients that characterize the temperature dependence of the self continuum. Continuum properties determined in the analysis of SGP cases are then validated using AERI measurements from the high-PWV MAO data set, which is especially informative with respect to the properties of the crucial self continuum.

The retrieval of water vapor continuum properties in the infrared window begins with baseline LBLRTM calculations of downwelling surface radiances for all the cases in the SGP AERI data set. These initial LBLRTM calculations utilize MT_CKD_4.1.1+BL (i.e., corresponding to the green results in Figure 9), although the retrieval results are fairly insensitive to this choice. Using the measurement-calculation residuals, for each AERI channel between 780 and 1,280 cm^{-1} a least-squares retrieval is performed of three independent variables—two linear scale factors, one each for the self and foreign continuum coefficients used in the LBLRTM calculations, and a scale factor for the exponent of the self continuum temperature dependence. The sensitivities of the residuals to changes in the retrieved continuum properties (i.e., the Jacobian) used in the retrieval are obtained from additional sets of LBLRTM calculations in which each of these three properties is perturbed by a small amount. In the methodology, we apply the PWV binning discussed above. That is, at each spectral point a single residual and corresponding sensitivities are computed for each PWV bin by averaging the "inner half" of the residuals for all the cases in that bin. With this, each least-square retrieval operates on 43 (the number of PWV bins) measurement-

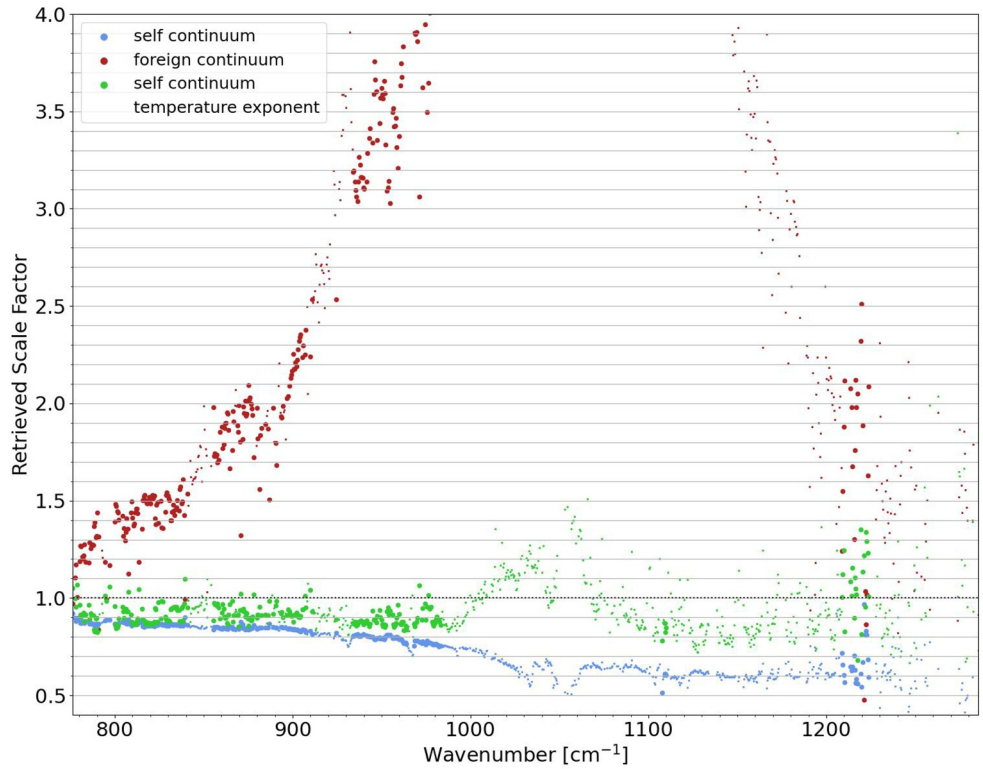

Figure 10. Scale factor values (relative to MT_CKD_4.1.1+BL) obtained from the initial retrieval step described in Section 4.3 for the self continuum (blue), foreign continuum (red), and self continuum temperature exponent (green).

calculation residuals. A three-variable retrieval is run to obtain scale factors for the self continuum, foreign continuum, and temperature exponent of the self continuum. Figure 10 shows the results of this retrieval.

Using these results, an interim revised version of the MT_CKD water vapor continuum is created by smoothing the retrieved spectral coefficients, interpolating through the ozone band region, and blending the retrieved values into the continuum values in neighboring regions. Then the entire retrieval process is repeated, including new sensitivity calculations using the interim MT_CKD version. This process is iterated until no further smoothly varying change in the continuum parameters could further improve the results (i.e., the median residuals and the linear and quadratic coefficients of the fit of the residuals with respect to PWV).

The median values of the measurement-calculation residuals using the final retrieved continuum coefficients and temperature dependence (MT_CKD_4.2_closure) are shown in pink in Figure 9a. As before, a quadratic function is fitted to these residuals at each spectral point, and the fit coefficients are shown in Figures 9b and 9c. Figure 8 shows in pink the quadratic fit for MT_CKD_4.2_closure for the same example AERI channels shown in this figure for prior versions of MT_CKD. The properties of the residuals between the SGP AERI measurements and LBLRTM residuals are greatly improved when MT_CKD_4.2_closure is used in the calculations compared to previous continuum versions. This improvement has resulted from increasing the atmospheric opacity for low PWV cases (roughly PWV <2 cm) while decreasing it for higher PWVs.

4.4. Validation Using AERI Observations From MAO

As for the SGP analysis above, median residuals (Figure 11) are computed from the inner-half mean residuals of each PWV bin for the set of MAO AERI cases. (Each MAO PWV bin has a width of 0.2 cm.) As for SGP, no bias correction is applied to the MAO AERI measurements. (For the warm and moist conditions of MAO, any such correction would have only a small impact.) Due to the limited range of PWV values in the MAO data set, quadratic functions are not fitted to the residuals. It is clear from Figure 11 that the residuals using MT_CKD_4.2_closure are greatly improved compared to previous continuum versions.

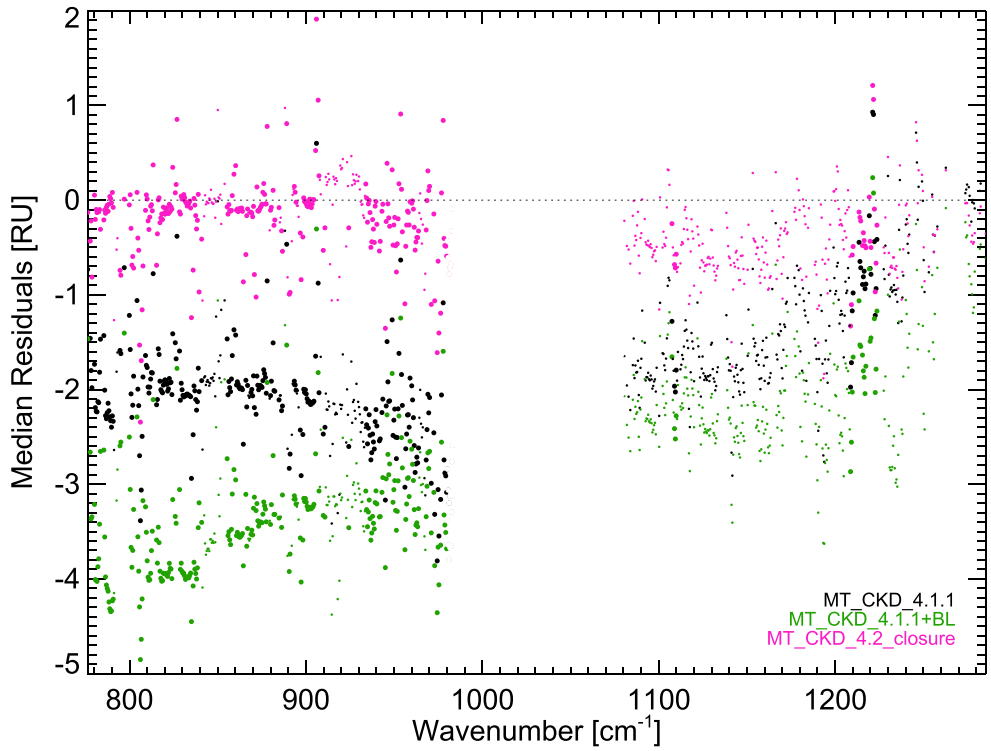

Figure 11. Median of the PWV-binned residuals between AERI measurements at MAO and corresponding LBLRTM calculations for the spectral region 780–1,280 cm^{-1}. The residual for each spectral point in a precipitable water vapor bin is computed as the mean of the "inner half" of all residuals in that bin, as described in Section 4.2. Residuals are shown for MT_CKD_4.1.1 (black), MT_CKD_4.1.1+BL (green), and MT_CKD_4.2_closure (pink).

The self and foreign continuum coefficients retrieved from the SGP AERI measurements in this study are shown (MT_CKD_4.2_closure) in purple in Figure 2d and pink in Figure 4, respectively. The retrieved temperature exponents of the self continuum are shown in Figure 3 (purple). Detailed discussion of these results is provided in Section 5.

4.5. An Adjustment to the Retrieved Foreign Continuum

4.5.1. Possible Issue With the Derived Foreign Continuum

The continuum coefficient retrieval described above did not include the spectral region from 990 to 1,070 cm^{-1}, which has significant ozone absorption. In Figure 4, a reasonable spectral continuation of the AERI-derived foreign continuum coefficients across this region is shown with a thin pink curve segment. The overall flatness of the foreign continuum coefficients in the 900–1,150 cm^{-1} region does not agree with the corresponding relative behavior of the coefficients derived by Baranov and Lafferty (2012) or that of MT_CKD_4.1.1, both of which have much smaller continuum coefficients in the middle of this region (~1,070 cm^{-1}) than at its endpoints. For MT_CKD_4.1.1, this deep well is a natural consequence of the assumption that the continuum in this region is due to the sum of transitions centered hundreds of wavenumbers away from this window region (e.g., at 100 cm^{-1}), with the continuum absorption from each transition decaying rapidly with increasing wavenumber far (e.g., 800–1,000 cm^{-1}) from its center. Based on its generally flat behavior from 900 to 1,150 cm^{-1}, we conclude that the MT_CKD_4.2_closure (pink) curve in Figure 4 may not represent the actual behavior of the foreign continuum in this region.

The optical depths in this region from the MT_CKD_4.2_closure foreign continuum are small. Figure 12a shows the derived foreign continuum optical depths at 980 cm^{-1} for the daytime cases in the SGP data set. For a PWV of 2 cm, this optical depth is ~0.03. At SGP, if there existed an atmospheric constituent with a small optical depth that scaled somewhat linearly with PWV, then the impact in our analysis of such a constituent would be to inflate

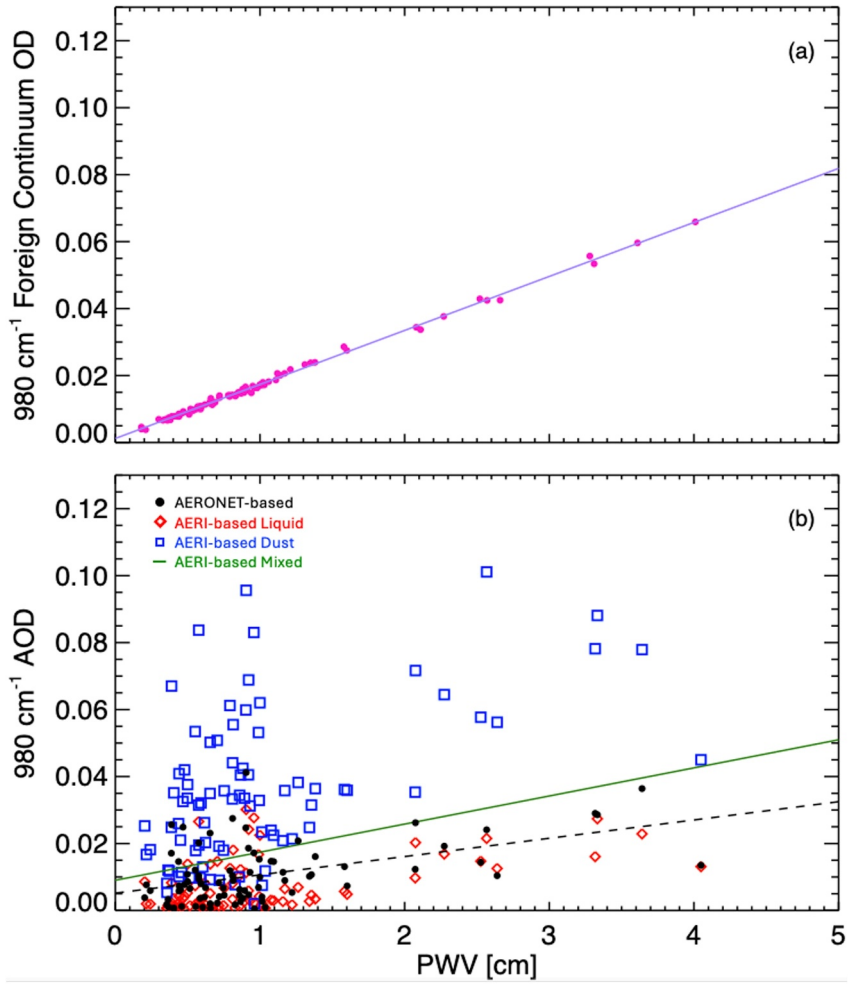

Figure 12. As a function of precipitable water vapor (PWV) for the daytime Southern Great Plains AERI cases analyzed in this study: (a) Foreign continuum optical depths from MT_CKD_4.2_closure; (b) Aerosol optical depths at 980 cm^{-1} derived from AERONET measurements assuming a combination of a deliquescent aerosol and mineral dust (black points with dashed black fitted line), retrievals from AERI observations at 2,500–2,860 cm^{-1} assuming a hydrated sulfate aerosol (modeled as liquid, red diamonds), retrievals from AERI observations at 2,500–2,860 cm^{-1} assuming montmorillonite spheres (dust, blue squares), and a 74/26 combination of the liquid and dust aerosol assumptions, respectively (green linear fit, individual values not shown for figure clarity). Positive correlation with PWV is seen for all modeled aerosols.

the derived foreign continuum optical depth above the actual foreign continuum, and this artificial inflation would disproportionately affect the derived foreign continuum most where it is smallest, that is, the 980–1,120 cm^{-1} region.

4.5.2. A Correction for the Possible Contribution of Aerosols

We now explore the possibility that the presence of aerosols in the skies over SGP can lead to such an overestimation of the foreign continuum in our analysis. We obtain retrievals of aerosol optical depth (AOD) with two markedly different approaches. We analyze periods coincident with the daytime cases in our data set and assume that the daytime result are representative of the entire data set.

The first approach is to retrieve AOD and aerosol refractive index (RI) within 1 hour of the AERI observations at SGP used in our analysis from the Aerosol Robotic Network (AERONET; Dubovik & King, 2000). We estimate the AOD at ~1,000 cm^{-1} (10 μm) from AERONET observations at shortwave infrared (longest wavelength observed is 1,640 nm) and visible wavelengths coupled with assumptions about aerosol composition. We assume that the AOD at longer wavelengths is dominated by contributions from an external mixture of coarse-mode

aerosols composed of deliquescent aerosol (produced through hygroscopic growth) and mineral dust. The RI of deliquescent aerosol converges with that of water, 1.3 at 1,640 nm and 1.2 + 0.05i at 10 μm. The RI of dust depends on the composition, which is assumed to be iron-oxide/hematite, a common soil component for the SGP region, having an index of refraction of about 1.6 at 1,640 nm and 2 + 0.02i at 10 μm. We allow the retrieved real part of the RI which spans the range from 1.3 to 1.6 μm to dictate the relative fraction of deliquescent aerosol to dust, and thus infer the effective RI of the external mixture at 10 μm. Lastly, we use Mie scattering theory to extend the measured AOD from shorter wavelengths out to ~10 μm. Clearly, the deliquescent components should have a positive dependence on relative humidity and PWV, a fact that is borne out in Figure 12b. The aerosol Angstrom exponent, which typically varies between +2 and 0 at the shorter wavelengths that are observed by the AERONET system, are be moderately negative (−0.65) over the 1,000–1,100 cm^{-1} spectral range, driven by changes in the refractive indices that vary notably in the longer wavelength range while being virtually constant at shorter wavelengths.

The AOD values obtained from this analysis are shown as black circles in Figure 12b. The results in Figure 12 show the estimated AOD at 980 cm^{-1} is approximately half of the derived foreign continuum optical depth. The aerosol optical depths scale reasonably linearly with PWV, a consequence of the hygroscopicity of ambient aerosol whereby aerosols increase in size through uptake of water vapor from the atmosphere, supporting the inference that the presence of aerosols could have impacted our retrieval of foreign continuum coefficients.

The second approach to retrieve AOD uses the downwelling radiance observations made by the AERI in the 2,500–2,860 cm^{-1} (3.5–4.0 μm) spectral region. Since at 2,500–2,860 cm^{-1} the downwelling AERI radiance observation is dominated by scattered solar radiation during the daytime, in this analysis we use only the daytime AERI samples that coincide with the AERONET observations used in the first approach. We apply the physical-iterative mixed-phase cloud retrieval algorithm (MIXCRA; Turner, 2005) to these AERI observations assuming that the "cloud" was composed of aerosol particles (as was done in Turner, 2008). We apply MIXCRA with two distinct assumptions for aerosol type: one, modeling the aerosol as liquid droplets (representing a hydrated sulfate aerosol, shown as red diamonds in Figure 12b), and the other assuming montmorillonite spheres (i.e., dust, blue squares in Figure 12b). The Interagency Monitoring of Protected Visual Environments (IMPROVE; Malm et al., 1994) project provides measurements of the mass of sulfate and soil particles that have diameters less than 2.5 μm. Based on IMPROVE data from Stilwell, OK (the closest IMPROVE site to ARM SGP during 2016–2018), over our analysis period, the mean ratio of the sulfate (liquid) aerosol mass to the sum of the sulfate and soil mass is determined to be 0.74. We thus estimate the AOD at 980 cm^{-1} using $0.74 * AOD_{liquid} + 0.26 * AOD_{dust}$, which yields somewhat higher AOD results (green line in Figure 12b) as a function of PWV as the first method that was based on AERONET observations.

These AOD estimates establish that it is plausible that the presence of aerosols has impacted the determination of the MT_CKD_4.2_closure foreign continuum coefficients shown in Figure 4. However, the assumptions about aerosol properties made in the analyses above are quite speculative and the actual aerosol optical depths in the infrared window may differ significantly from those we derived. The possibility that our continuum coefficient retrieval has been impacted by aerosols leaves us with two choices, each of which has positive aspects and flaws. We could ignore this likely contamination of our derived foreign continuum (MT_CKD_4.2_closure in Figure 4) and its problematic flat spectral behavior, and provide these foreign continuum coefficients in the next release of MT_CKD. This choice, when used in concert with our derived self continuum, would provide radiative closure with the AERI observations used in this study, but likely only because the water vapor continuum in this region inappropriately included some absorption that is actually due to aerosols. The other choice is to use the analysis above to make an estimate of the aerosol contribution to the derived foreign continuum, subtract this initial estimate of this aerosol contamination from MT_CKD_4.2_closure, and then use the MT_CKD line shape methodology (Mlawer et al., 2012) to compute foreign continuum coefficients that are in reasonable agreement with this difference. By construction, this option would have relative spectral behavior in the middle of the window that is similar to the behavior in MT_CKD_4.1.1 (also similar to that measured by Baranov & Lafferty, 2012), but would no longer provide closure with the AERI measurements since calculations using this foreign continuum would be missing optical depth unless a user explicitly included longwave aerosols in their calculation. Another drawback of this approach stems from the realization that any estimate of aerosol absorption in the infrared window would be highly uncertain, which would lead to significant uncertainty in the foreign continuum derived after the aerosol contribution is removed from the MT_CKD_4.2_closure foreign continuum.

Given this difficult choice, we feel that it is important for the MT_CKD continuum model to provide our best estimate of the actual foreign continuum despite the inherent uncertainty of the approach used to derive it. Therefore, we choose to derive the new foreign continuum for MT_CKD_4.2 by accounting for the estimated contribution of aerosols. Given that the use of MT_CKD_4.2 will not result in radiative closure, we will also provide the MT_CKD_4.2_closure foreign continuum as an alternate foreign continuum choice for users of MT_CKD.

In Appendix B, we discuss the approach used to derive a specification of the foreign continuum in the infrared window that is consistent with both (a) the closure analysis described in Section 4.2 interpreted in light of the aerosol absorption analysis above (i.e., in Figure 12b) and (b) the relative spectral behavior of the foreign continuum in this region given by the MT_CKD line shape calculation. This derivation uses the MT_CKD line shape formalism to compute foreign continuum coefficients from 780 to 1,250 cm^{-1} that, once subtracted from the coefficients in MT_CKD_4.2_closure, is roughly consistent with the properties (AOD and Angstrom exponent in the infrared window) of the aerosol absorption derived from the AERONET measurements.

4.5.3. The Adjusted Foreign Continuum

The foreign continuum coefficients (labeled as MT_CKD_4.2) that result from this aerosol-removing procedure are shown as a purple curve in Figure 4. Since a similar line shape formalism was used to derive these coefficients as was done for MT_CKD_1.0 (virtually the same as MT_CKD_4.1.1), the MT_CKD_4.2 coefficients also have a minimum near 1,100 cm^{-1}. The spectral behavior of the MT_CKD_4.2 coefficients now more closely resemble the Baranov and Lafferty (2012) measurements than the derived coefficients before the assumed impact of aerosols was accounted for. This agreement with an independent measurement of foreign continuum absorption provides a measure of confidence that the aerosol adjustment has some validity.

A few observations are worth pointing out. First, calculations using MT_CKD_4.2 do not provide radiative closure with either the SGP or MAO AERI observations. As shown in Figure 9, impressive agreement between the observations and calculations is obtained using MT_CKD_4.2_closure, but this closure to some extent is due to the assumed inclusion of the radiative effects of aerosols in that continuum version. Removing that contribution, as has been done to construct MT_CKD_4.2, destroys that radiative closure. Therefore, a comparison between the observations and calculations using MT_CKD_4.2 is not informative and we do not include those results in Figure 9. Second, the strong agreement shown in Figure 11 between the MAO AERI measurements and calculations using MT_CKD_4.2_closure occurs even though that continuum version is assumed to include the impact of aerosols at SGP. This is possibly due to reasonably similar aerosol loading at SGP and MAO, both continental sites, and the reduced relative radiative impact of aerosols at MAO compared to SGP given the higher PWV amounts at MAO. Third, some consideration should be given to the results for MT_CKD_4.1.1 and MT_CKD_4.1.1+BL in Figure 9 in light of the need for the aerosol adjustment detailed above. In both cases, the foreign coefficients in the infrared window in these continuum versions were not derived from field studies, so they could not have been impacted by aerosols in the same way that the MT_CKD_4.2_closure coefficients are assumed to have been. The window self continuum used in these calculations (the same in both versions) was derived by Turner et al. (2004), a radiative closure field study at SGP. It is reasonable that atmosphere opacities in this previous study were affected by a similar aerosol loading as in the current study, and that the self continuum coefficients derived in Turner et al. (2004) implicitly include the radiative effects of the aerosols. Therefore, no further adjustment to these versions is needed to evaluate the behavior of their associated residuals, and it is fair to compare them to those obtained using MT_CKD_4.2_closure, as is done in Figure 9.

4.6. Uncertainty Analysis

The determination of the uncertainties in our retrieved values of self continuum coefficients, foreign continuum coefficients, and the temperature dependence of the self continuum in the infrared window is challenging. Consideration must be given to typical uncertainties in radiative closure studies, such as those due to the radiometric instrument and the specification of the atmospheric profile, as well as complexities in this study such as the consideration of the role of aerosols in the derivation of the foreign continuum. We here provide an analysis of key sources of uncertainty in our derived continuum values.

For our uncertainty analysis, we consider to what extent the retrieved continuum values can be modified while maintaining "good agreement" between the measurements and calculations. How we define "good agreement"

must reflect the uncertainties in both the measurements and calculations. The total uncertainty in the radiance residuals at each spectral point provides a foundation for evaluating alternate sets of continuum values. If the residuals generally stay within the radiance residual uncertainty values for all PWV bins, then any alternate values are considered plausible. Using this approach, we can find limits past which good agreement is no longer possible, therefore defining the uncertainty in each continuum parameter.

Sources of uncertainty in the radiance residuals arise from the uncertainty in (a) the specification of trace gas abundances, (b) the temperature and water vapor profiles, and (c) the AERI radiance measurements. The method used to determine the uncertainty due to the trace gas specification is discussed above and is shown in Figure 7a. The uncertainty due to temperature and water vapor profiles is evaluated through the use of a reasonable alternate specification of these profiles (see Section 3.3). Figure 7b shows the spectral RMS differences between calculations that use these alternate profiles and those that use the profiles employed in the analysis described above. Finally, the AERI uncertainty is assigned a value of 0.1 RU based on the random error spectra of the instrument, as estimated by the calibration equation used in its processing (Knuteson et al., 2004b; Revercomb et al., 1988).

In addition, it is clear from Figure 8 that there is variability in the final (pink) residuals as a function of PWV. To account for this additional source of uncertainty, we compute the interquartile differences of the binned residuals for each spectral point, which is shown in Figure 7c, and include this as an additional term in the uncertainty calculations.

We assume that these four sources of uncertainty in the residuals are independent and add these values in quadrature at each spectral point (total shown as black circles in Figure 7d). Since the determination of continuum coefficients enforces a degree of spectral smoothness on the coefficients, we group the uncertainty values in 20 cm^{-1} intervals. We take a conservative approach in assigning the final uncertainty value in each interval by using the RMS of the spectral values, which are also shown in Figure 7d.

Now we compute alternate sets of continuum coefficients at each spectral point to determine the maximum that each continuum coefficient can be perturbed while keeping the residuals as a function of PWV within the uncertainty in the residuals computed above. We illustrate this procedure for the self continuum. First, all self continuum coefficients in MT_CKD_4.2_closure are increased, in turn, by 5%, 10%, 20%, and 30%. For each perturbation, we then follow the procedure detailed in Section 4.2 to derive optimal spectral values for the foreign continuum and the temperature dependence of the self continuum. For illustration, quadratic fits to the resulting residuals from these optimal perturbations are shown in Figure 13 as a function of PWV for all spectral elements in the 20 cm^{-1} bins that contain the wavenumbers in Figure 13, as well as the 1,200–1,220 cm^{-1} bin. (The wavenumber corresponding to each curve shown is not identified since this analysis is being performed collectively for the spectral elements grouped in each interval.) As an example, Figure 13f shows that, for the 940–960 cm^{-1} region, the coefficients obtained starting with a 5% perturbation to the self continuum result in the residuals staying within the unshaded region, which corresponds to the radiance uncertainty in this region. That is, a 5% perturbation to the self continuum results in measurement-calculation agreement (as defined above). In contrast, the curves corresponding to a 10% perturbation (Figure 13g) do not remain within the unshaded region, so a 10% change to the self continuum does not lead to agreement. Based on the set of perturbation calculations, for this spectral region we determine that the self continuum uncertainty is 7%. We perform this analysis for all 20 cm^{-1} bins—the resulting self continuum uncertainty values are shown as thin purple error bars on the MT_CKD_4.2 curve in Figure 2.

We repeat this procedure starting with a series of foreign continuum perturbations, determining optimal spectral values for the self continuum and the temperature dependence of the self for each perturbation. This results in the foreign continuum uncertainty values shown in Figure 4 for MT_CKD_4.2_closure in the 20 cm^{-1} spectral bins. Note that in some spectral regions (primarily the ozone-dominated region from 980 to 1,080 cm^{-1}) this method is not able to determine a reliable uncertainty value for the foreign continuum due to the large uncertainty in the residuals and combined behavior of the self continuum and its temperature dependence in response to the foreign perturbations. In this region, we compute an uncertainty by combining the uncertainty at its boundaries (i.e., 970 and 1,090 cm^{-1}) with the difference in continuum values resulting from alternate reasonable ways to span the gap in retrieved (i.e., MT_CKD_4.2_closure) foreign continuum values from 980 to 1,080 cm^{-1}. We discuss below the uncertainty associated with the MT_CKD_4.2 foreign continuum coefficients.

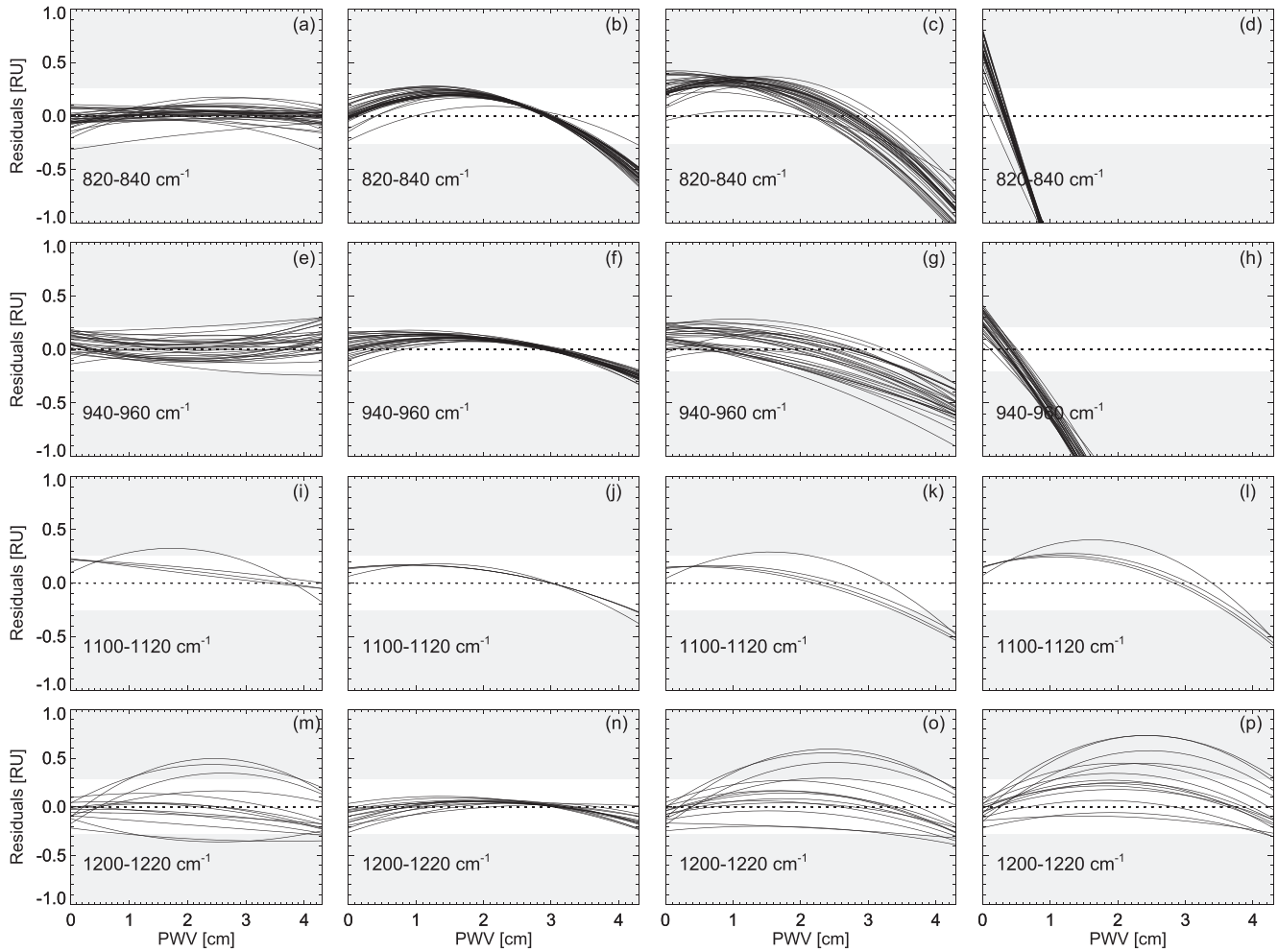

Figure 13. For four example 20 cm^{-1} spectral regions, quadratic fits to the residuals are shown for MT_CKD_4.2 closure (left column) and variations in which the self continuum has been increased by 5% (middle left column), 10% (middle right column), and 20% (right column), with the foreign continuum and self continuum temperature dependence rederived for each perturbation (as described in Section 4.6). Curves are shown for the spectral elements corresponding to the large circles in Figure 9 and not all curves are shown on all panels for clarity. The regions shaded gray on each panel are outside of the total uncertainty for the respective panels. A set of curves that does not stay mostly within the unshaded region indicates that the corresponding perturbation to the self continuum is greater than the self continuum uncertainty in that spectral region.

Finally, we follow this procedure beginning with a series of perturbations to the temperature dependence of the self continuum, determining optimal spectral values for the self and foreign continuum. However, in all spectral bins this method is not able to derive reliable estimates of the uncertainty in the self continuum temperature dependence. Even though the AERI data sets used in our study are not able to effectively constrain the self continuum temperature dependence, below we consider the results of other studies to determine rough estimates of the uncertainty in the MT_CKD_4.2 temperature dependence parameters.

The continuum parameters derived from the AERI measurements are not independent—for example, an increase in the derived self continuum value at a spectral point would necessitate a lower associated foreign continuum value in order to maintain overall radiative closure at that point. Therefore, for the uncertainty analysis it is informative to understand how these two continuum values covary. We therefore perform a retrieval of the foreign continuum value for a small perturbation to the self continuum (with the temperature dependence kept fixed) for all SGP cases in this study. Figure 14 shows the median ratios of the foreign and self continuum changes in these retrievals for the window region. Consideration of the uncertainty in either of these quantities should be done in the context of their combined behavior.

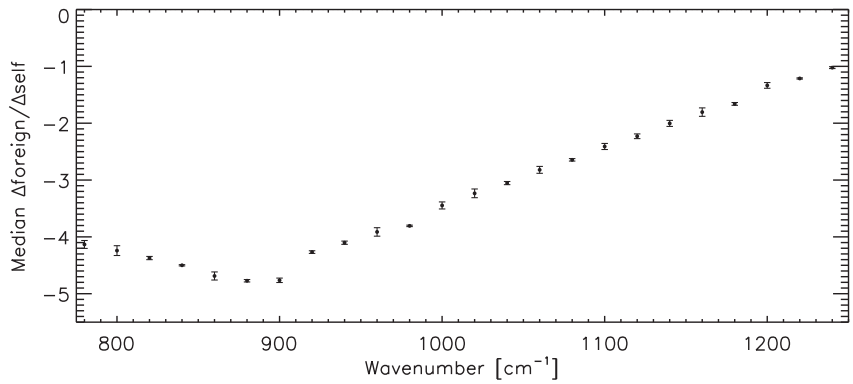

Figure 14. For all Southern Great Plains cases, median ratio (interquartile range shown with bars) of the change in derived foreign continuum value to a small perturbation in the self continuum value.

The above derivation of uncertainty values for the MT_CKD_4.2_closure foreign continuum coefficients does not directly apply to the MT_CKD_4.2 foreign continuum, which was derived using information other than the AERI measurements at SGP and MAO. The method used to derive these foreign continuum coefficients was quite speculative, involving (a) the MT_CKD_4.2_closure foreign continuum coefficients, (b) "best guess" estimates of the aerosol optical properties in the infrared window, and (c) a calculation using the MT_CKD line shape formulation constrained to foreign continuum values outside the infrared window and those inferred in the window from (a) and (b). The highly conjectural nature of this approach presents large challenges from using it alone to determine reasonable uncertainty estimates. Instead, we use all available information (MT_CKD_4.2 closure uncertainties, analysis of the method used to derive MT_CKD_4.2 foreign continuum, and the laboratory measurements shown in Figure 4) to provide users of MT_CKD with a rough estimate of the uncertainty of MT_CKD_4.2 in specifying water vapor foreign continuum absorption in this region. The upper limit of the uncertainty must reflect the possibility that the impact of aerosols on the derivation of foreign continuum is negligible (i.e., in contrast to the significant AOD values shown in Figure 12b), so the corresponding uncertainty values are determined by the difference between MT_CKD_4.2 and MT_CKD_4.2_closure (accounting for its own uncertainty). Reassuringly, even though this uncertainty estimate did not consider the single-frequency measurement of Cormier et al. (2005), the upper envelope of the MT_CKD_4.2 uncertainty estimates (shown with thin purple vertical bars in Figure 4) allows the possibility that the foreign continuum is as great as that value. With respect to the lower limit of the MT_CKD_4.2 uncertainty, we explicitly consider the results from the Baranov and Lafferty (2012) study, which is generally lower than the MT_CKD_4.2 coefficients but clearly represent possibly valid values. We compute the uncertainty by adding in quadrature: (a) the difference between MT_CKD_4.2 and MT_CKD_4.1.1+BL and (b) the uncertainty in the coefficients determined in Baranov and Lafferty (2012). The resulting MT_CKD_4.2 uncertainty estimates are generally consistent with the results we would have attained in our study had we adjusted the MT_CKD_4.2_closure coefficients to account for the impact of aerosol optical depths somewhat greater than we actually assumed (i.e., consistent with the relative aerosol loading of the green line compared to the black line in Figure 12b). In Figure 4, we denote MT_CKD_4.2 foreign continuum uncertainty estimates with open-ended vertical lines to contrast the broader perspective used to determine these values with the AERI-based uncertainty estimates used for the MT_CKD_4.2_closure foreign coefficients, which are denoted as (pink) vertical lines with end caps. To conclude, MT_CKD users should be aware of possible considerable uncertainties when utilizing MT_CKD_4.2 foreign continuum coefficients.

With a similar perspective, we also consider all available information to determine rough uncertainty estimates for the MT_CKD_4.2 self continuum temperature dependence exponents, which are not able to be effectively constrained by the AERI measurements used in this study. The upper limit of the uncertainty needs to include the (refit) values from the Burch and Alt (1984) study (accounting for that study's uncertainty) since we view its results with confidence due to the close agreement of its derived self continuum coefficients with those from the current study. (See Figure 2.) When considering the lower limit of possible values of the temperature dependence exponents, we do not consider the values derived by Baranov et al. (2008) with great confidence since the self continuum coefficients determined in that work do not agree with those derived in the current study. As a result,

there is little information to go on to constrain the lower uncertainty limit. We therefore define the uncertainty bars to be equal in the positive and negative directions (adjusted to ignore the bump in the MT_CKD_4.2 exponents centered at 780 cm^{-1}).

5. Analysis of MT_CKD_4.2

Figure 2a shows the final self continuum coefficients (MT_CKD_4.2) derived in this study along with previous versions of the continuum model. With MT_CKD_4.1.1 used as a reference, Figure 2d shows the relative spectral behavior of MT_CKD_4.2 (and its uncertainty), the most recent laboratory measurements from three groups, previous versions of CKD and MT_CKD based on field studies that have been adjusted (as described in Section 2) to account for a larger foreign continuum than utilized in their respective original derivations, and the similarly adjusted results from the field study by Taylor et al. (2003). Although these self continuum specifications do not all agree, it can be argued the evidence clearly suggests that MT_CKD_4.1.1 is too strong across the entire infrared window. For wavenumbers less than 900 cm^{-1}, most of the results shown agree that the self continuum is 8%–15% weaker than MT_CKD_4.1.1. Exceptions to this are the study of Baranov et al. (2008) and the adjusted coefficients of CKD_2.1, which is based on the Westwater et al. (1995) study. The adjustment made to CKD_2.1 only accounts for a change in the foreign continuum, but another significant bias in the Westwater et al. (1995) results is likely present. The type of sonde used in the calculations in that study to specify the water vapor fields were subsequently shown to have a dry bias of 4%–8% due to contamination of the relative humidity sensor by the packaging (Turner et al., 2003; Wang et al., 2002). Given the squared dependence of the self continuum on water vapor abundance, a rough estimate suggests that the self continuum coefficients derived in that study were likely too high by at least 8%. As a result, the CKD_2.1_adj curve in Figure 2d likely needs to be shifted downward by that amount to account for this bias. Given that, all results shown in Figure 2d for 780–900 cm^{-1} exhibit agreement except for a single outlier result by Baranov et al. (2008). The good agreement of these self continuum specifications persists over the rest of infrared window with the exception of MT_CKD_1.0_adj, which is based on the adjusted results of the Turner et al. (2004) study. It is encouraging that the accurate cavity ring down measurement by Cormier et al. (2005) agrees within the tight uncertainty bound of the current study. In spectral regions in which the uncertainty estimates of the current study are small, the results of the current study are in agreement with all laboratory measurements by Burch and Alt (1984) and most of the adjusted values from the Taylor et al. (2003) field analysis.

The MT_CKD_4.2 foreign continuum coefficients, which have been adjusted to account for the presence of aerosols at SGP as described in Section 4.5, are shown in Figure 4. Since its behavior near its minimum results from a similar line shape calculation as MT_CKD_1.0, it is not surprising that the shapes of these two continuum versions are similar in this region. However, MT_CKD_4.2 is ~5 times greater than its predecessor in the 960–1,150 cm^{-1} region, and 2–4 times greater in the regions of the infrared window outside this minimum region, that is, where the continuum is stronger and the AERI observations provide a greater constraint. In these regions, the MT_CKD_4.2 uncertainty estimates do not include the MT_CKD_1.0 (equivalent to MT_CKD_4.1.1) coefficients. Despite the quite speculative approach used to adjust the derived foreign continuum for aerosols, there is some correspondence of these continuum values with the Baranov and Lafferty (2012) experimental values. By construction, the MT_CKD_4.2 uncertainty estimates include the Baranov and Lafferty (2012) values.

The self continuum temperature dependence exponents derived in this study are shown in Figure 3. Also shown in Figure 3 are the exponents in MT_CKD_4.1.1 as well as values derived from the laboratory studies of Baranov et al. (2008), Cormier et al. (2005), and Burch and Alt (1984). (It is important to note that the exponents shown on this figure for these studies are for the continuum coefficients as defined in MT_CKD, which are specified for a reference density and do not include the radiation term.) The Burch and Alt (1984) study is represented by two sets of alternate temperature exponent values: one based on the data in the table provided in that work associated with its Figure 2, and one based on our analysis of the plotted values in its Figure 2. It is clear from Figure 3 that there is no consensus between the specifications of the self continuum temperature exponents that are displayed. The MT_CKD_4.2 values are in excellent agreement at the single location analyzed in Cormier et al. (2005) and are closer than MT_CKD_4.1.1 to the Baranov et al. (2008) values in the region where the AERI analysis is most definitive. Above 980 cm^{-1}, the MT_CKD_4.2 exponents diverge from the Baranov et al. (2008) values, but there

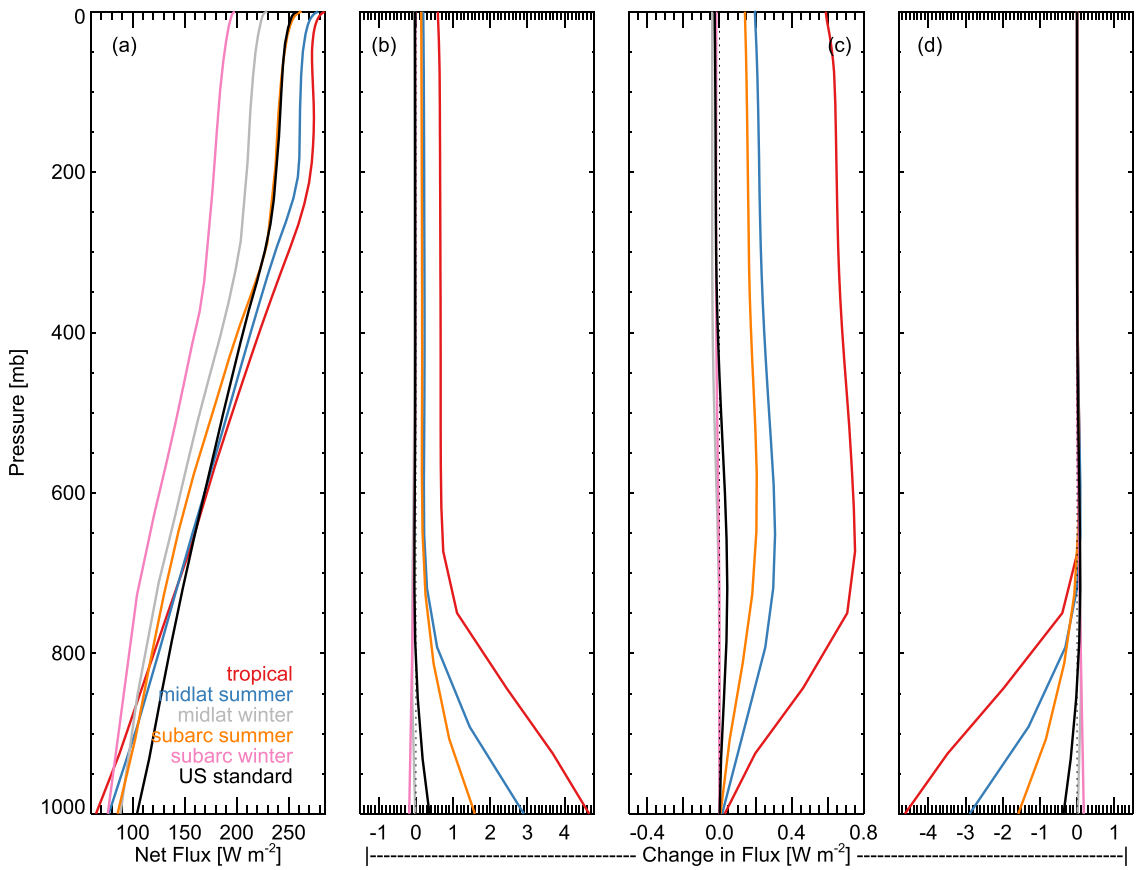

Figure 15. For six standard atmospheres: (a) longwave net flux from LBLRTM calculations using MT_CKD_4.1.1; (b) Difference in net flux between calculations that use MT_CKD_4.2 and calculations that use MT_CKD_4.1.1; (c) Difference in upward flux between MT_CKD_4.2 and MT_CKD_4.1.1; (d) Difference in downward flux between MT_CKD_4.2 and MT_CKD_4.1.1.

is some suggestion in Figure 10 that a justifiable choice could have been made to decrease the MT_CKD_4.2 exponents further, thereby bringing them in closer agreement to Baranov et al. (2008). Our inability to determine uncertainty values for the exponents based on the AERI analysis alone reflects that a wide range of exponent values are able (after adjustments to the self and foreign coefficients) to provide radiative closure with the observations within the uncertainty in the residuals. Therefore, the exponent values shown in Figure 3 should be considered numerical values that optimize the radiative closure results rather than an attempt at a definitive determination of the spectral behavior of a physical quantity.

6. Impact

6.1. Broadband Fluxes and Heating Rates

The impact of the modified water vapor continuum in MT_CKD_4.2 on broadband radiative fluxes (Figure 15) depends strongly on the moisture content of a profile. (See Table 1 for PWV values.) For dry winter profiles, the continuum modifications cause a modest decrease in upward flux and an increase in downward flux from the increased opacity due to the larger foreign continuum, which outweighs the decrease in the self continuum. The difference in downwelling flux sharply increases at ~800 mb for the tropical or summer profiles (Figure 15d). In the tropical atmosphere, for example, the downwelling flux at the surface decreases by more than 4 W/m^2 as a result of the overall decrease in atmospheric opacity in the IR window caused by the 10%–30% decrease in the dominant water vapor self continuum. The magnitude of the change in upwelling flux (Figure 15c) due to the use of MT_CKD_4.2 is much smaller than for the downwelling flux since the radiating temperature of lower atmosphere, the region in which the self continuum emits radiation, does not differ too greatly from the surface

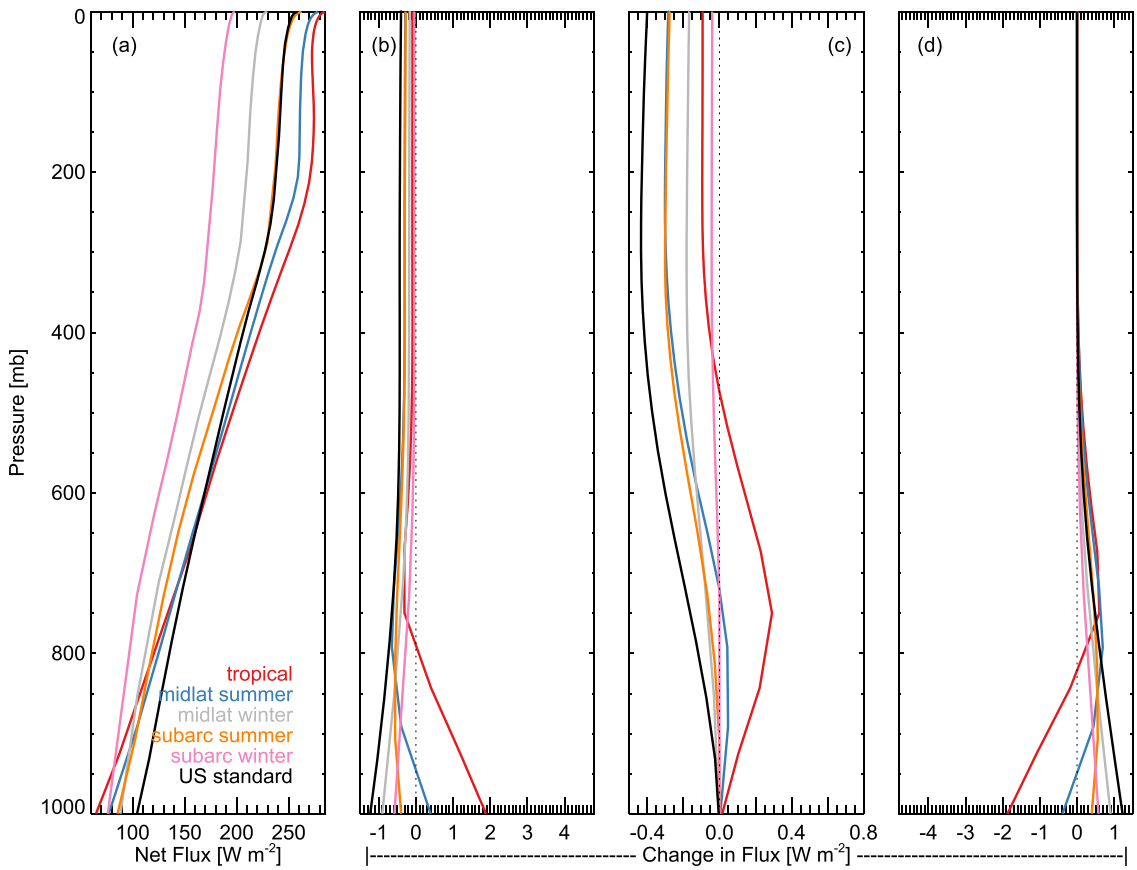

Figure 16. Same as Figure 15, but differences in panels (b–d) are for calculations that use MT_CKD_4.2_closure and those that use MT_CKD_4.1.1.

temperature. Therefore, decreased absorption of surface-emitted radiation by the self continuum in MT_CKD_4.2 is partially compensated by its decreased emission of the lower atmosphere at a (typically) slightly lower temperature. Nevertheless, the upwelling radiation does increase by ~0.7 W/m^2 in the mid-troposphere and 0.5 W/m^2 at the top of the tropical atmosphere, with smaller but still notable increases for atmospheres with moderate PWV values.

The analysis in this study shows that the total atmospheric opacity in the infrared window is less than had previously been thought, but the exact partitioning between the water vapor continuum and aerosols, that is, the difference between MT_CKD_4.2 and MT_CKD_4.2_closure, is quite uncertain. Figure 16, which shows the analogous results to those in Figure 15 for calculations using MT_CKD_4.2_closure, may better reflect the impact on fluxes resulting from this study since all sources of opacity in the infrared window are accounted for. In drier conditions the increase in atmospheric opacity in MT_CKD_4.2_closure results in an increase in downwelling flux at the surface, consistent with the change in the measurement-calculation residuals (e.g., Figure 8) for similarly low PWVs. For higher PWV cases, the decreased overall absorption, driven by the decrease in the optical depth of the dominant self continuum, results in a decrease in surface downwelling flux. For upwelling flux at TOA, all cases shown in Figure 16 show a decrease due to the continuum changes. Even for moist cases in which the magnitude of the increase in foreign continuum optical depth is less than the decrease in the self continuum, the change in foreign continuum results in an upwelling flux difference of larger magnitude since foreign continuum emission occurs higher in the atmosphere, that is, at temperatures that differ more with respect to the surface temperature than the self continuum emission temperature. Crucially, the impact on fluxes may be very different when the aerosol properties (e.g., loading) differ greatly from the aerosols at the location analyzed in this study since the presumed contribution of aerosols is included in the foreign continuum in these calculations.

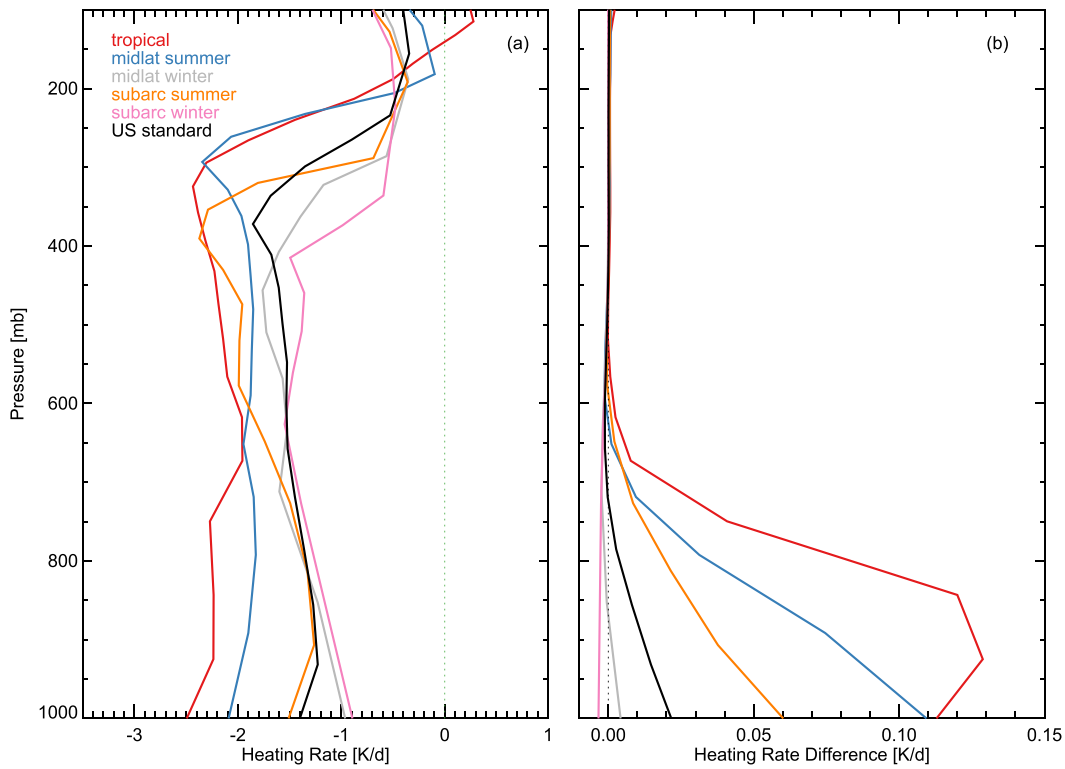

Figure 17. For six standard atmospheres: (a) longwave heating rates from LBLRTM calculations using MT_CKD_4.1.1 and (b) difference in heating rates between calculations that use MT_CKD_4.2 and calculations that use MT_CKD_4.1.1.

Figure 17 shows the difference in longwave heating rates due to modifications in MT_CKD_4.2. The largest changes occur in moist atmospheres, with the heating rates increasing (less cooling) by ∼5% in the lower layers of the atmospheres. Figure S1 in Supporting Information S1 presents analogous results for MT_CKD_4.2_closure.

6.2. Top of the Atmosphere Brightness Temperature

Figure 18 shows the change in the brightness temperature at the top of the atmosphere between LBLRTM calculations that use MT_CKD_4.2 and those that use MT_CKD_4.1.1. These differences increase with the PWV of the atmospheric profile, with maximum of ∼+0.3 K for the tropical atmosphere, and do not show a great deal of spectral variability throughout the infrared window. This suggests that use of the new continuum version (v4.2) will lead to a non-trivial change in surface temperatures retrieved using satellite radiances in the infrared window. Figure S2 in Supporting Information S1 provides analogous results for MT_CKD_4.2_closure. For all but the moistest of the profiles shown, the change in brightness temperature is negative due to the additional absorption provided by the aerosol assumed to be included in the foreign continuum.

6.3. Climate Considerations

Since only a small fraction of the radiative forcing due to carbon dioxide and methane occurs in the infrared window, the change in the water vapor continuum derived in this work will result in only a very small change in these forcings. Therefore, these forcing changes are not shown here.

We assess the impact of the new continuum and resulting opacity change in the infrared window on climate feedbacks with radiative calculations for idealized atmospheric profiles (see, e.g. Koll & Cronin, 2018) using a range of surface temperatures from 240 to 340K (in 5K increments). Atmospheric temperatures follow a moist adiabat until reaching 220K (defined as the tropopause); temperatures above the tropopause are fixed at 220K. Relative humidity in the troposphere is 75%, carbon dioxide abundance is set to 395 ppm, and ozone

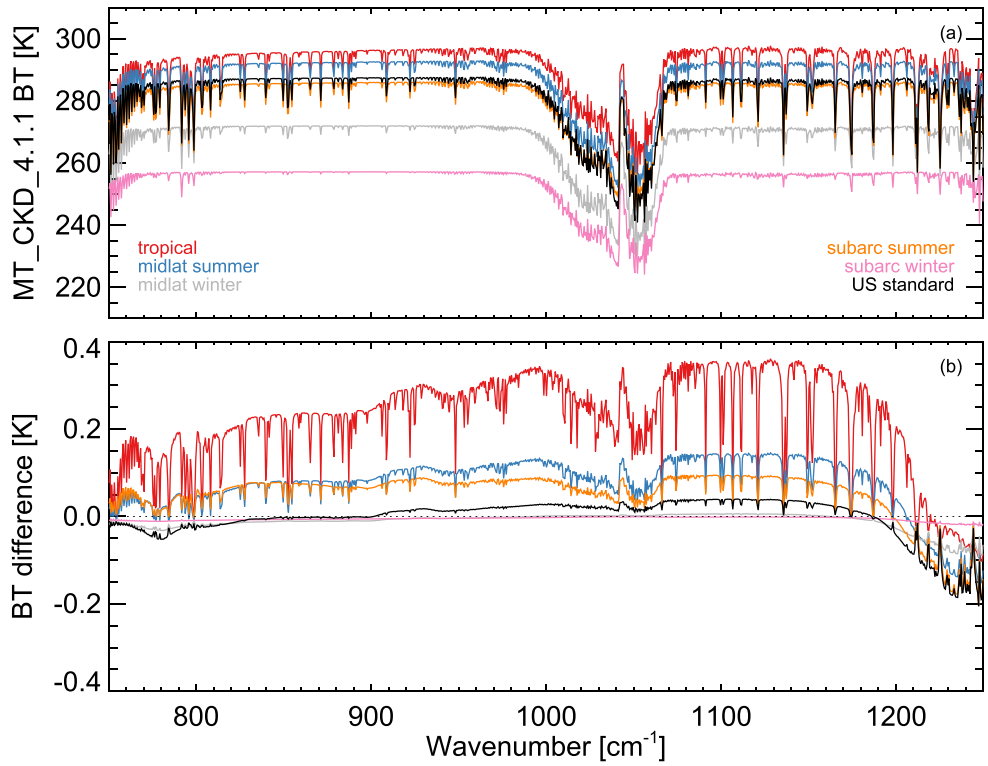

Figure 18. For six standard atmospheres: (a) brightness temperatures calculated with LBLRTM with MT_CKD_4.1.1 and (b) brightness temperature differences between calculations that use MT_CKD_4.2 and calculations that use MT_CKD_4.1.1.

concentrations are based on the U.S. Standard atmosphere (ozone concentrations are zero above the tropopause and rescaled in the troposphere to ensure the same total column amount at all surface temperatures). The change in flux between consecutive surface temperatures is interpreted as the climate feedback. Figure 19 shows this feedback as determined with the existing water vapor continuum (v4.1.1, dashed curves) and with the newly derived continuum (v4.2, solid curves). Differences are shown in the lower panels. Changes to the continuum, and the resulting decrease in atmospheric opacity in the infrared window, induce an increase in climate feedback of ∼5% at current surface temperature (∼290K), rising to greater than 10% for a surface temperature of ∼300K.

The colored curves in Figure 19 show the contributions of key spectral regions to the total climate feedback. (For this figure, we have slightly expanded the spectral region defined as the window to include the entire region in which the continuum has been modified in this study.) At current Earth temperatures, the infrared window (green) is the spectral region with by far the largest climate feedback. Secondary contributions to the total climate feedback are also provided by infrared water vapor absorption bands, the CO_2 ν_2 band at 15 μm (600–750 cm^{-1}), and the main infrared ozone band at 9.6 μm (1,000–1,070 cm^{-1}). The climate feedback in the infrared window region decreases with surface temperature due to the increase in atmospheric opacity in moister atmospheres. This opacity increase is rapid due to the dominant role of the water vapor self continuum in the window region and its quadratic dependence on water vapor concentration. The decrease in the climate feedback in the infrared window for higher surface temperatures is partially compensated for by increases in the climate feedback in water vapor absorption bands and the CO_2 band, which has the largest contribution for surface temperatures larger than ∼307K.

Figure 19 shows the significant increase in climate feedback in the infrared window due to the continuum changes derived in this study. The reduced opacity in the revised water vapor continuum results in the climate feedback in the infrared window becoming negative at a temperature 3K greater than before this revision. Our calculations do not extend to sufficiently high temperatures for the climate feedback for the complete longwave region (black curve) to become negative (i.e., runaway greenhouse), but Figure 19 suggests that the revised continuum implies

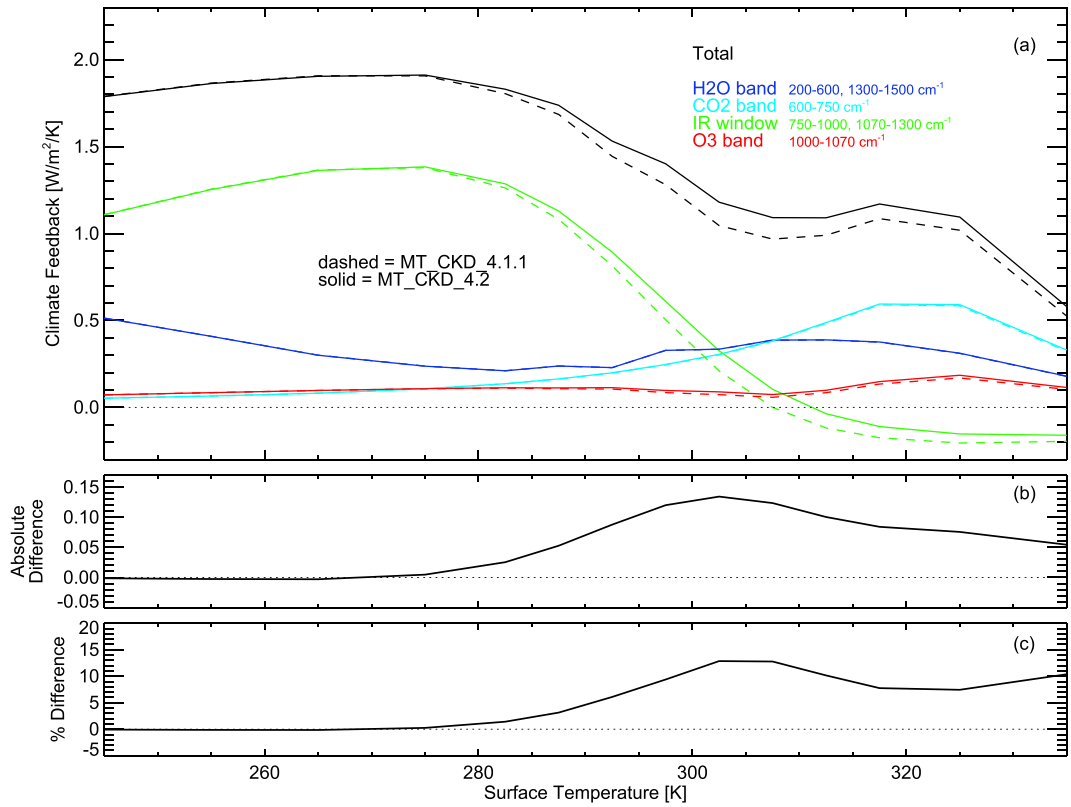

Figure 19. As a function of surface temperature in moist adiabat profiles (as described in Section 6.3), (a) climate feedback for full longwave region (black), water vapor absorption bands (blue), CO_2 ν_2 band (cyan), infrared window (green), and ozone band (red). Solid curves use revised continuum (MT_CKD_4.2) in the calculations while dashed curves use previous continuum (MT_CKD_4.1.1); (b) for full longwave, climate feedback differences between calculations using MT_CKD_4.2 and MT_CKD_4.1.1; and (c) percentage differences in climate feedback between calculations using MT_CKD_4.2 and MT_CKD_4.1.1. Climate feedback is defined as the change in TOA flux per unit change in surface temperature.

that runaway greenhouse conditions will occur on Earth at a slightly higher temperature than had been previously thought. (Analogous results to those presented in Figure 19 can be seen in Figure S3 in Supporting Information S1 for MT_CKD_4.2_closure.)

Figure 20b shows spectrally-resolved climate feedbacks computed with MT_CKD_4.2, while Figure 20c shows the climate feedback differences for MT_CKD_4.2 with respect to MT_CKD_4.1.1; analogous results for MT_CKD_4.2_closure are shown in Figure S4 in Supporting Information S1. (For clarity, in these and similar figures we show only the results corresponding to 10K increments of surface temperature.) Since the changes to the continua decrease absorption due to the self continuum, which is the dominant source of opacity in this region, with the new continuum the climate feedback is increased throughout the vast majority of the infrared window region. The exception is in the region 1,200–1,300 cm^{-1} for low surface temperatures (i.e., lower PWV values) where, under these conditions, the increased absorption due to the revised foreign continuum can outweigh the impact of the reduced self continuum, leading to a decrease in opacity and a slight increase in climate feedback. Figure 20c indicates that the change in climate feedback varies spectrally and with surface temperature, a result of the varying spectral behavior of the continuum changes and atmospheric opacity for the different surface temperatures. Additional discussion about the climate feedback results in Figures 19 and 20 is provided in Section S2 in Supporting Information S1.

Changes resulting from the new continuum formulation to the surface net radiative flux (defined positive upwards), key to processes such as evaporation, are shown in Figure 21 as a function of surface temperature for these moist adiabatic calculations; spectral results are shown in Figure S5 in Supporting Information S1. Analogous results for MT_CKD_4.2_closure are shown in Figures S6 and S7 in Supporting Information S1, respectively.

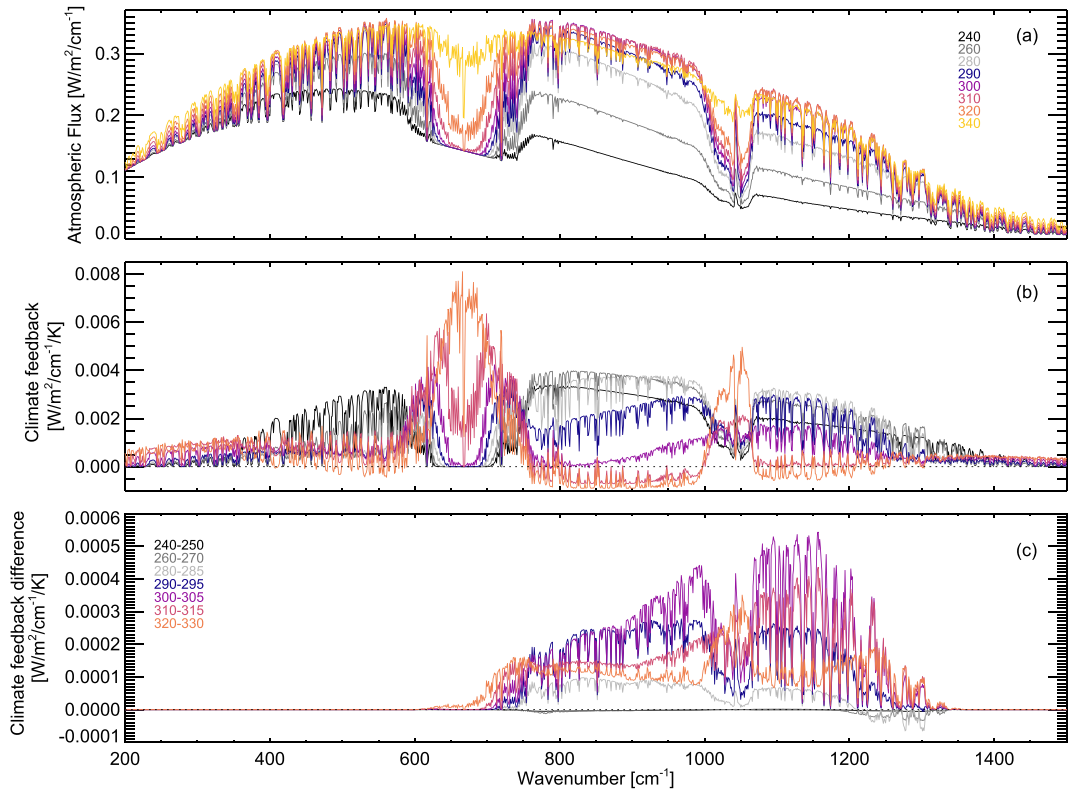

Figure 20. For various surface temperatures (colored curves) in moist adiabat profiles (as described in Section 6.3): (a) TOA longwave flux calculated using MT_CKD_4.2; (b) spectral behavior of climate feedback calculated for the temperature ranges denoted on panel (c); and (c) spectral climate feedback differences between calculations using MT_CKD_4.2 and MT_CKD_4.1.1.

The results in Figure 21 reflect a balance between the increase in upwelling surface flux with increasing surface temperature and an increase in downwelling surface flux due to the increased atmospheric temperature and water vapor loadings associated with the increased surface temperature. At low surface temperature, the low water vapor amounts lead to the former term being larger, so the sensitivity of net surface flux to surface temperature (the "surface climate feedback") is positive. When the surface temperature is larger than 270K, the impact of the increase in atmospheric opacity associated with a greater surface temperature becomes increasing large, leading to a negative surface climate feedback. The magnitude of this feedback, dominated by the infrared window region, continues to increase with surface temperature until ~300K. At higher temperatures, the most opaque part of this region (~800 cm^{-1}) has become sufficiently opaque so that its surface net flux is small and, therefore, the change in surface net flux values resulting from a change in surface temperature decreases. These spectral regions stop contributing appreciably to the surface climate feedback, and the overall magnitude starts to decrease. This trend continues as the surface temperature increases until the surface net flux approaches zero, as does the surface climate feedback.

The impact of the changes to the infrared window continuum is to decrease the magnitude of the surface climate feedback for lower surface temperatures, where the trend in surface climate feedback is due to the increase in surface downwelling flux due to the increased atmospheric opacity—the decrease in the self continuum slows down this trend. Conversely, for higher temperatures, the decrease in self continuum opacity decelerates the trend of the surface net flux approaching zero, thereby leading to an increase in the magnitude of the surface climate feedback.

For completeness, Section S2 in Supporting Information S1 includes analogous figures (both for MT_CKD_4.2 and 4.2_closure) for the atmospheric net flux (TOA minus surface net flux) for the moist adiabat calculations, change in atmospheric net flux due to the change in surface temperature ("atmospheric climate feedback"), and

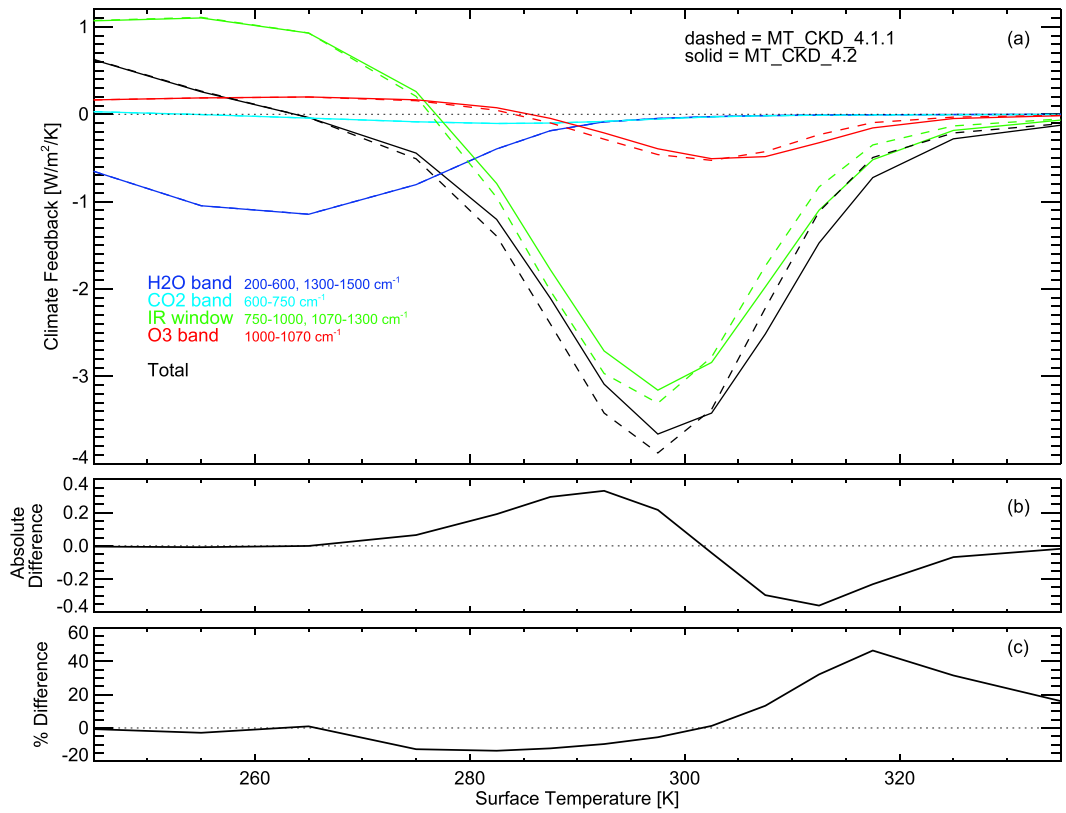

Figure 21. Similar to Figure 19 but for the surface instead of TOA. Surface climate feedback is defined as the change in surface net flux (defined as positive upward) per unit change in surface temperature.

changes in this feedback due to the revised water vapor continuum in the infrared window (Figures S8–S11 in Supporting Information S1).

7. Conclusion

This study provides a new determination of the strength of water vapor continuum absorption in the infrared atmospheric window, which, despite its importance to climate, has not been the subject of many observational studies in the last two decades. Our results are consistent with several recent analyses that indicate that the self continuum, the dominant source of atmospheric absorption in this spectral region, is too strong in MT_CKD_4.1.1. In general, the weaker self continuum derived here results in an overall increase in atmospheric transparency in the window in MT_CKD_4.2 compared to MT_CKD_4.1.1. However, the high transparency in atmospheres with low amounts of water vapor may slightly decreases due to the increase in foreign continuum absorption derived in this study. The continuum changes implemented in MT_CKD_4.2 lead to a significant decrease (~4.5 W/m^2) in downwelling longwave flux at the surface for moist atmospheres as well as a modest increase (~0.6 W/m^2) in OLR. The increased fraction of surface-leaving radiation that escapes to space leads to a notable increase (~5–10%) in the clear-sky climate feedback.

The diversity of the continuum values derived in previous studies is striking, and the high uncertainty of some of the continuum values we have derived means that our study cannot resolve all remaining uncertainties of significance related to the infrared window in Earth's radiative budget and climate. This is especially the case for the foreign continuum and the temperature dependence of the self continuum, but also for the self continuum in certain spectral regions (e.g., 1,150–1,200 cm^{-1}). This reality points to the need for further accurate laboratory studies of the water vapor continuum in the infrared window. Within the last year, an important step in this direction has occurred. Motivated by a presentation of preliminary results from this study (Mlawer, 2022), the Campargue group at the University of Grenoble Alpes undertook a measurement of the self continuum at ~1,185 cm^{-1} using the accurate technique of optical feedback cavity ring down spectroscopy. The results of this

study (Fournier et al., 2024; F24) are consistent with our result that there is a need for a significant reduction in the strength of the MT_CKD_4.1.1 self continuum in this region, although the decrease derived in our study is greater than in F24. The two results agree within the uncertainties associated with our determination of the self continuum in this region. Measurements of the self continuum were performed in F24 over a limited range of temperatures (296–308 K), which resulted in the determination that the temperature dependence is much weaker than the value we have implemented in MT_CKD_4.2. Given that our study determined that the self continuum temperature dependence could assume a wide range of values while still allowing radiative closure with AERI measurements, this is not surprising. There is a clear need for additional accurate laboratory studies of the self continuum across the full atmospheric window, as well as its temperature dependence and the strength of foreign continuum absorption.

The foreign continuum analysis in this study also demonstrates the need for further laboratory studies of this source of atmospheric absorption. In this study, we posit that our derivation of foreign continuum absorption includes a contribution from aerosols and determine the spectrally dependent fraction of the absorption due to the foreign continuum versus aerosols through a highly speculative approach. Despite the resulting substantial uncertainty inherent our methodology, our results point out the possibly important role that aerosol absorption may play in the longwave radiative budget, which we hope will prompt further study.

Appendix A

The method to estimate the "adjusted" self continuum values shown in Figure 2d for three previous field studies is described here. Using the SGP data set described in Section 3, we retrieved self continuum values (see Section 4.2 for the description of the methodology) using the MT_CKD_4.1.1+BL foreign continuum. For our reconsideration of the Turner et al. (2004) study, we used the entire data set to estimate the change in derived self continuum values due to the modified foreign continuum, while for the tropical analyses upon which CKD_2.1 was based (Han et al., 1997; Westwater et al., 1995) we used only the most moist cases in the SGP data set. These revised self continuum values are shown in Figure 2d as MT_CKD_1.0_adj and CKD_2.1_adj, respectively. Also shown in this figure are the self continuum values derived in a field study by Taylor et al. (2003), which assumed the CKD_2.4 foreign continuum, and corresponding self continuum values that are estimated as the values that would have been obtained had the larger MT_CKD_4.1.1+BL foreign continuum values been assumed instead (denoted as "Taylor_adj").

Appendix B

Based on (a) the foreign continuum value at 980 cm^{-1} from a revised line shape fit (similar to the one used to derive MT_CKD_1.0 as described in Mlawer et al., 2012) applied to the foreign continuum coefficients in MT_CKD_4.1.1 from 500 to 800 cm^{-1} and (b) the value of the foreign continuum at 980 cm^{-1} in MT_CKD_4.2_closure, we estimate that the actual foreign continuum is a little more than half of the retrieved foreign continuum at 980 cm^{-1} and assume that aerosols are responsible for the remaining fraction. This split between foreign continuum and aerosol is weighted more to the foreign continuum than is implied by Figure 12, but is within the uncertainty of the AOD estimates in panel b of that figure. The first step in the procedure to account for the estimated impact of aerosols on the derived spectral foreign continuum coefficients is to compute the spectral fraction of the derived continuum due to aerosol optical depths. To do this, the spectral dependence of the AOD is assumed to be given by a derived Angstrom exponent of −0.647 while the combined foreign and AOD is given by MT_CKD_4.2_closure. Using this ratio, the estimated aerosol contribution is removed from the derived foreign continuum coefficients, yielding an estimate of the actual foreign continuum coefficients (i.e., with aerosol removed). It is important to note that since no coefficients were derived from 990 to 1,070 cm^{-1}, this gap remains in these estimated pure continuum coefficients. These coefficients are then used as constraints in a new fit of the same line shape formalism that was used to derive MT_CKD_1.0. The new fit is aimed at providing values for the foreign continuum in the gap as well as in neighboring spectral regions that are impacted greatly by aerosols (given our assumption) and, therefore, the derived foreign continuum coefficients in those regions cannot be considered very definitive (e.g., 1,080–1,150 cm^{-1}). The main priorities in the fitting effort are to match the following properties of the constraining foreign continuum coefficients: (a) the overall slope of the coefficients from 800 to 980 cm^{-1} and (b) the coefficient values in spectral regions closest to the gap in which the actual foreign continuum value are thought to be responsible for more than 60% of the AERI-derived foreign continuum

coefficients (960–980 cm^{-1} and 1,220–1,230 cm^{-1}). The continuum coefficients resulting from this fit are the final foreign continuum coefficients in the targeted spectral region; in neighboring spectral regions the coefficients from the fit are smoothly merged with the constraining coefficients (i.e., AERI-derived), resulting in the final foreign water vapor coefficients from this AERI analysis (780–1,250 cm^{-1}). In spectral regions just outside of this range, these coefficients are transitioned into the existing MT_CKD_4.1.1 foreign continuum coefficients in spectral regions (<600 cm^{-1}, >1,400 cm^{-1}) in which the coefficients have been determined in previous observation-based analyses.

Data Availability Statement

All SGP and MAO observations (Atmospheric Radiation Measurement, 1993a, 1993b, 2001, 2004a, 2004b, 2004c, 2014a, 2014b, 2014c, 2014d, 2014e) used in this study were obtained from https://www.arm.gov/data. The LBLRTM radiative transfer model (1991), including the version used in this study (v12.15.1) can be accessed from https://github.com/AER-RC/LBLRTM and the MT_CKD continuum model (2003) from https://github.com/AER-RC/MT_CKD. The LBLRTM input files derived from ARM observations that are used in this study can be found in a tar file that can be downloaded from Zenodo (https://zenodo.org/records/10909710). The Zenodo file also contains all aerosol-related data used in our analysis, as well as the code (Python) used to retrieve the self and foreign continuum coefficients and the self continuum temperature exponents from the measurement-calculation residuals. Additional supporting information is also available in this tar file.

Acknowledgments
The primary support for this project at AER was provided by the Atmospheric Systems Research (ASR) program of the U.S. Department of Energy under contract number DE-SC0018296. Additional support for the analysis and dissemination of the results were provided by the NASA U.S. Participating Investigator program under contract number 80NSSC21K1038 and the National Science Foundation under award number 1916927. Support at NOAA was provided by ASR contract 89243019SSC000034. We thank the DOE Atmospheric Radiation Measurement program for the observations upon which this study is based and for their excellent data archive. AER authors are indebted to Karen Cady-Pereira, Matt Alvarado, and Rick Pernak for helpful advice. Part of this research was carried out at the Jet Propulsion Laboratory, California Institute of Technology, under a contract with NASA (80NM0018D0004). We thank three anonymous reviewers for their comments and perspectives.

References

Anderson, G. P., Clough, S. A., Kneizys, F. X., Chetwynd, J. H., & Shettle, E. P. (1986). AFGL atmospheric constituent profiles (0.120 km). (No. AFGL-TR-86-0110). Air Force Geophysics Lab, Hanscom, AFB, MA. Retrieved from http://www.dtic.mil/docs/citations/ADA175173

Atmospheric Radiation Measurement (ARM) user facility. (1993a). Microwave radiometer (MWRLOS). March 2016 to October 2018, Southern Great Plains (SGP) Central Facility, Lamont, OK (C1). Compiled by M. Cadeddu, V. Morris and M. Tuftedal [Dataset]. *ARM Data Center*. https://doi.org/10.5439/1999490

Atmospheric Radiation Measurement (ARM) user facility. (1993b). Surface meteorological instrumentation (MET). March 2016 to October 2018, Southern Great Plains (SGP) Lamont, OK (extended and co-located with C1) (E13). Compiled by J. Kyrouac, Y. Shi and M. Tuftedal [Dataset]. *ARM Data Center*. https://doi.org/10.5439/1786358

Atmospheric Radiation Measurement (ARM) user facility. (2001). Balloon-borne sounding system (SONDEWNPN). March 2016 to October 2018, Southern Great Plains (SGP) Central Facility, Lamont, OK (C1). Compiled by E. Keeler, K. Burk and J. Kyrouac [Dataset]. *ARM Data Center*. https://doi.org/10.5439/1595321

Atmospheric Radiation Measurement (ARM) user facility. (2004a). Atmospheric Emitted Radiance Interferometer (AERICH1). March 2016 to October 2018, Southern Great Plains (SGP) Central Facility, Lamont, OK (C1). Compiled by J. Gero, H. Revercomb, D. Turner, J. Taylor, R. Garcia, D. Hackel, B. Ermold and K. Gaustad [Dataset]. *ARM Data Center*. https://doi.org/10.5439/1989299

Atmospheric Radiation Measurement (ARM) user facility. (2004b). Atmospheric Emitted Radiance Interferometer (AERICH2). March 2016 to October 2018, Southern Great Plains (SGP) Central Facility, Lamont, OK (C1). Compiled by J. Gero, H. Revercomb, D. Turner, J. Taylor, R. Garcia, D. Hackel, B. Ermold and K. Gaustad [Dataset]. *ARM Data Center*. https://doi.org/10.5439/1989302

Atmospheric Radiation Measurement (ARM) user facility. (2004c). Atmospheric Emitted Radiance Interferometer (AERIENGINEER). March 2016 to October 2018, Southern Great Plains (SGP) Central Facility, Lamont, OK (C1). Compiled by J. Gero, H. Revercomb, D. Turner, J. Taylor, R. Garcia, D. Hackel, B. Ermold and K. Gaustad [Dataset]. *ARM Data Center*. https://doi.org/10.5439/1989301

Atmospheric Radiation Measurement (ARM) user facility. (2014a). Balloon-borne sounding system (SONDEWNPN). January 2014 to October 2015, ARM Mobile Facility (MAO) Manacapuru, Amazonas, Brazil; AMF1 (M1). Compiled by E. Keeler, K. Burk and J. Kyrouac [Dataset]. *ARM Data Center*. https://doi.org/10.5439/1595321

Atmospheric Radiation Measurement (ARM) user facility. (2014b). Microwave radiometer (MWRLOS). January 2014 to October 2015, ARM Mobile Facility (MAO) Manacapuru, Amazonas, Brazil; AMF1 (M1). Compiled by M. Cadeddu, V. Morris and M. Tuftedal [Dataset]. *ARM Data Center*. https://doi.org/10.5439/1999490

Atmospheric Radiation Measurement (ARM) user facility. (2014c). Surface meteorological instrumentation (MET). January 2014 to October 2015, ARM Mobile Facility (MAO) Manacapuru, Amazonas, Brazil; AMF1 (M1). Compiled by J. Kyrouac, Y. Shi and M. Tuftedal [Dataset]. *ARM Data Center*. https://doi.org/10.5439/1786358

Atmospheric Radiation Measurement (ARM) user facility. (2014d). Atmospheric Emitted Radiance Interferometer (AERIENGINEER). January 2014 to October 2015, ARM Mobile Facility (MAO) Manacapuru, Amazonas, Brazil; AMF1 (M1). Compiled by J. Gero, H. Revercomb, D. Turner, J. Taylor, R. Garcia, D. Hackel, B. Ermold and K. Gaustad [Dataset]. *ARM Data Center*. https://doi.org/10.5439/1989301

Atmospheric Radiation Measurement (ARM) user facility. (2014e). Atmospheric Emitted Radiance Interferometer (AERICH1). January 2014 to October 2015, ARM Mobile Facility (MAO) Manacapuru, Amazonas, Brazil; AMF1 (M1). Compiled by J. Gero, H. Revercomb, D. Turner, J. Taylor, R. Garcia, D. Hackel, B. Ermold and K. Gaustad [Dataset]. *ARM Data Center*. https://doi.org/10.5439/1989299

Baranov, Y. I., & Lafferty, W. J. (2012). The water vapor self- and water–nitrogen continuum absorption in the 1000 and 2500 cm^{-1} atmospheric windows. *Philosophical Transactions of the Royal Society A: Mathematical, Physical and Engineering Sciences*, *370*(1968), 2578–2589. https://doi.org/10.1098/rsta.2011.0234

Baranov, Y. I., Lafferty, W. J., Ma, Q., & Tipping, R. H. (2008). Water vapor continuum absorption in the 800–1250 cm^{-1} spectral region at temperatures from 311 to 363K. *Journal of Quantitative Spectroscopy and Radiative Transfer*, *109*(12–13), 2291–2302. https://doi.org/10.1016/j.jqsrt.2008.03.004

Burch, D. E. (1982). Continuum absorption by H_2O. In *AFGL-TR-81-0300* (p. 46). Air Force Geophys. Lab., Hanscom AFB. https://doi.org/10.1117/12.931899

Burch, D. E., & Alt, R. L. (1984). Continuum absorption by H2O in the 700–1200 cm^{-1} and 2400–2800 cm^{-1} windows. In *AFGL-TR-84-0128* (p. 32). Air Force Geophys. Lab., Hanscom AFB.

Cadeddu, M. P., Liljegren, J. C., & Turner, D. D. (2013). The atmospheric radiation measurement (ARM) program network of microwave radiometers: Instrumentation, data, and retrievals. *Atmospheric Measurement Techniques*, *6*(9), 2359–2372. https://doi.org/10.5194/amt-6-2359-2013

Clough, S. A., Kneizys, F. X., & Davies, R. W. (1989). Line shape and the water vapor continuum. *Atmospheric Research*, *23*(3–4), 229–241. https://doi.org/10.1016/0169-8095(89)90020-3

Clough, S. A., Shephard, M. W., Mlawer, E. J., Delamere, J. S., Iacono, M. J., Cady-Pereira, K., et al. (2005). Atmospheric radiative transfer modeling: A summary of the AER codes. *Journal of Quantitative Spectroscopy and Radiative Transfer*, *91*(2), 233–244. https://doi.org/10.1016/j.jqsrt.2004.05.058

Cormier, J. G., Ciurylo, R., & Drummond, J. R. (2002). Cavity ringdown spectroscopy measurements of the infrared water vapor continuum. *Journal of Chemical Physics*, *116*(3), 1030–1034. https://doi.org/10.1063/1.1425825

Cormier, J. G., Hodges, J. T., & Drummond, J. R. (2005). Infrared water vapour continuum absorption at atmospheric temperatures. *Journal of Chemical Physics*, *122*(11), 114309. https://doi.org/10.1063/1.1862623

Delamere, J. S., Clough, S. A., Payne, V., Mlawer, E. J., Turner, D. D., & Gamache, R. (2010). A far-infrared radiative closure study in the Arctic: Application to water vapor. *Journal of Geophysical Research*, *115*(D17), D17106. https://doi.org/10.1029/2009JD012968

Dubovik, O., & King, M. D. (2000). A flexible inversion algorithm for retrieval of aerosol optical properties from Sun and sky radiance measurements. *Journal of Geophysical Research*, *105*(D16), 20673–20696. https://doi.org/10.1029/2000jd900282

Feng, J., Paynter, D., & Menzel, R. (2023). How a stable greenhouse effect on Earth is maintained under global warming. *Journal of Geophysical Research: Atmospheres*, *128*(9), e2022JD038124. https://doi.org/10.1029/2022JD038124

Fournier, Q., Kassi, S., Mondelain, D., Fleurbaey, H., Georges, R., & Campargue, A. (2024). The water vapor self-continuum absorption at 8.45 μm by optical feedback cavity ring down spectroscopy. *Journal of Quantitative Spectroscopy and Radiative Transfer*, *315*. https://doi.org/10.2139/ssrn.4607109

Han, Y., Shaw, J. A., Churnside, J. H., Brown, P. D., & Clough, S. A. (1997). Infrared spectral measurements in the tropical Pacific atmosphere. *Journal of Geophysical Research*, *102*(D4), 4353–4356. https://doi.org/10.1029/96jd03717

Harries, J., Carli, B., Rizzi, R., Serio, C., Mlynczak, M., Palchetti, L., et al. (2008). The far-infrared Earth. *Reviews of Geophysics*, *46*(4), RG4004. https://doi.org/10.1029/2007RG000233

Jeevanjee, N., Koll, D. D., & Lutsko, N. (2021). "Simpson's law" and the spectral cancellation of climate feedbacks. *Geophysical Research Letters*, *48*(14), e2021GL093699. https://doi.org/10.1029/2021gl093699

Knuteson, R. O., Revercomb, H. E., Best, F. A., Ciganovich, N. C., Dedecker, R. G., Dirkx, T. P., et al. (2004a). Atmospheric Emitted Radiance Interferometer. Part I: Instrument design. *Journal of Atmospheric and Oceanic Technology*, *21*(12), 1763–1776. https://doi.org/10.1175/JTECH-1662.1

Knuteson, R. O., Revercomb, H. E., Best, F. A., Ciganovich, N. C., Dedecker, R. G., Dirkx, T. P., et al. (2004b). Atmospheric Emitted Radiance Interferometer. Part II: Instrument performance. *Journal of Atmospheric and Oceanic Technology*, *21*(12), 1777–1789. https://doi.org/10.1175/JTECH-1663.1

Koll, D. D., & Cronin, T. W. (2018). Earth's outgoing longwave radiation linear due to H_2O greenhouse effect. *Proceedings of the National Academy of Sciences*, *115*(41), 10293–10298. https://doi.org/10.1073/pnas.1809868115

Koll, D. D., Jeevanjee, N., & Lutsko, N. J. (2023). An analytic model for the clear-sky longwave feedback. *Journal of the Atmospheric Sciences*, *80*(8), 1923–1951. https://doi.org/10.1175/jas-d-22-0178.1

LBLRTM. (1991). Line-By-Line Radiative Transfer Model. Developed by S.A. Clough [Software]. *Atmospheric and Environmental Research, Radiation and Climate Group*. Retrieved from https://github.com/AER-RC/LBLRTM

Malm, W. C., Sislerm, J. F., Huffmann, D., Eldred, R. A., & Cahill, T. A. (1994). Spatial and seasonal trends in particle concentration and optical extinction in the United States. *Journal of Geophysical Research*, *99*(D1), 1347–1370. https://doi.org/10.1029/93JD02916

Martin, S. T., Artaxo, P., Machado, L., Manzi, A. O., Souza, R. A., Schumacher, C., et al. (2016). The Green Ocean Amazon experiment (GoAmazon2014/5) Observes Pollution affecting gases, aerosols, clouds, and Rainfall over the Rain forest. *Bulletin of the American Meteorological Society*, *98*(5), 981–997. https://doi.org/10.1175/bams-d-15-00221.1

Mascio, J., Turner, D., & Flynn, C. (2024). Data/code for Mlawer et al. 2024 (A more transparent infrared window) [Dataset]. *Zenodo*. https://doi.org/10.5281/zenodo.10909710

McKim, B. A., Jeevanjee, N., & Vallis, G. K. (2021). Joint dependence of longwave feedback on surface temperature and relative humidity. *Geophysical Research Letters*, *48*(18), e2021GL094074. https://doi.org/10.1029/2021gl094074

Mlawer, E. (2022). Recent development of the MT_CKD water vapor continuum. Invited talk at ASA-HITRAN 2022, Reims, France.

Mlawer, E. J., Cady-Pereira, K. E., Mascio, J., & Gordon, I. E. (2023). The inclusion of the MT_CKD water vapor continuum model in the HITRAN molecular spectroscopic database. *Journal of Quantitative Spectroscopy and Radiative Transfer*, *306*, 108645. https://doi.org/10.1016/j.jqsrt.2023.108645

Mlawer, E. J., Payne, V. H., Moncet, J.-L., Delamere, J. S., Alvarado, M. J., & Tobin, D. C. (2012). Development and recent evaluation of the MT_CKD model of continuum absorption. *Philosophical Transactions of the Royal Society A: Mathematical, Physical and Engineering Sciences*, *370*(1968), 2520–2556. https://doi.org/10.1098/rsta.2011.0295

Mlawer, E. J., Taubnam, S. J., Brown, P. D., Iacono, M. J., & Clough, S. A. (1997). RRTM, a validated correlated-k model for the longwave. *Journal of Geophysical Research*, *102*, 16663–16682.

Mlawer, E. J., & Turner, D. D. (2016). Spectral radiation measurements and analysis in the ARM program. *Meteorological Monographs*, *57*, 14.1–14.17. https://doi.org/10.1175/AMSMONOGRAPHS-D-15-0027.1

Mlawer, E. J., Turner, D. D., Paine, S. N., Palchetti, L., Bianchini, G., Payne, V. H., et al. (2019). Analysis of water vapor absorption in the far-infrared and submillimeter regions using surface radiometric measurements from extremely dry locations. *Journal of Geophysical Research: Atmospheres*, *124*(14), 8134–8160. https://doi.org/10.1029/2018JD029508

MT_CKD. (2003). Mlawer-Tobin_Clough-Kneizyzs-Davies Continum Model. Developed by E.J. Mlawer and S.A. Clough [Software]. *Atmospheric and Environmental Research, Radiation and Climate Group*. Retrieved from https://github.com/AER-RC/MT_CKD

Otsu, N. (1979). A threshold selection method from gray-level histograms. *IEEE Transactions on Systems, Man, and Cybernetics*, *9*(1), 62–66. https://doi.org/10.1109/TSMC.1979.4310076

Randles, C. A., da Silva, A. M., Buchard, V., Colarco, P. R., Darmenov, A., Govindaraju, R., et al. (2017). The MERRA-2 aerosol reanalysis, 1980 onward. Part I: System description and data assimilation evaluation. *Journal of Climate*, *30*(17), 6823–6850. https://doi.org/10.1175/JCLI-D-16-0613.1

Revercomb, H. E., Buijs, H., Howell, H. B., LaPorte, D. D., Smith, W. L., & Sromovsky, L. A. (1988). Radiometric calibration of IR Fourier transform spectrometers: Solution to a problem with the high-resolution interferometer sounder. *Applied Optics*, *27*(15), 3210–3218. https://doi.org/10.1364/ao.27.003210

Seeley, J. T., & Jeevanjee, N. (2021). H_2O windows and CO_2 radiator fins: A clear-sky explanation for the peak in equilibrium climate sensitivity. *Geophysical Research Letters*, *48*(4), e2020GL089609. https://doi.org/10.1029/2020gl089609

Shephard, M. W., Goldman, A., Clough, S. A., & Mlawer, E. J. (2003). Spectroscopic improvements providing evidence of formic acid in AERI-LBLRTM validation spectra. *Journal of Quantitative Spectroscopy and Radiative Transfer*, *82*(1–4), 383–390. https://doi.org/10.1016/S0022-4073(03)00164-X

Simpson, G. (1928). Some studies in terrestrial radiation. *Memoirs of the Royal Meteorological Society*, *2*(16), 69–95.

Sisterson, D. L., Peppler, R. A., Cress, T. S., Lamb, P. J., & Turner, D. D. (2016). The ARM Southern Great Plains (SGP) site. The atmospheric radiation measurement program: The first 20 years, meteorological monograph. *American Meteorological Society*, *57*, 6.1–6.14. https://doi.org/10.1175/AMSMONOGRAPHS-D-16-0004.1

Slingo, A., & Webb, M. J. (1997). The spectral signature of global warming. *Quarterly Journal of the Royal Meteorological Society*, *123*(538), 293–307. https://doi.org/10.1002/qj.49712353803

Taylor, J. P., Newman, S. M., Hewison, T. J., & McGrath, A. (2003). Water vapour line and continuum absorption in the thermal infrared – Reconciling models and observations. *Quarterly Journal of the Royal Meteorological Society*, *129*(2003), 2949–2969. https://doi.org/10.1256/qj.03.08

Turner, D. D. (2003). *Microphysical properties of single and mixed-phase Arctic clouds derived from ground-based AERI observations* (Ph.D. Dissertation). University of Wisconsin-Madison (p. 167). https://search.library.wisc.edu/catalog/999951770902121

Turner, D. D. (2005). Arctic mixed-phase cloud properties from AERI-lidar observations: Algorithm and results from SHEBA. *Journal of Applied Meteorology*, *44*(4), 427–444. https://doi.org/10.1175/jam2208.1

Turner, D. D. (2008). Ground-based retrievals of optical depth, effective radius, and composition of airborne mineral dust above the Sahel. *Journal of Geophysical Research*, *113*(D13), E00E03. https://doi.org/10.1029/2008JD010054

Turner, D. D., & Blumberg, W. G. (2019). Improvements to the AERIoe thermodynamic profile retrieval algorithm. *IEEE Selected Topics Appl. Earth Obs. Remote Sens.*, *12*(5), 1339–1354. https://doi.org/10.1109/JSTARS.2018.2874968

Turner, D. D. & Ellingson, R. G. (Eds.). (2016). *The atmospheric radiation measurement (ARM) program: The first 20 years* (Vol. 57). American Meteorological Society.

Turner, D. D., Lesht, B. M., Clough, S. A., Liljegren, J. C., Revercomb, H. E., & Tobin, D. C. (2003). Dry bias and variability in Vaisala radiosondes: The ARM experience. *Journal of Atmospheric and Oceanic Technology*, *20*(1), 117–132. https://doi.org/10.1175/1520-0426(2003)020<0117:dbaviv>2.0.co;2

Turner, D. D., & Löhnert, U. (2014). Information content and uncertainties in thermodynamic profiles and liquid cloud properties retrieved from the ground-based Atmospheric Emitted Radiance Interferometer (AERI). *Journal of Applied Meteorology and Climatology*, *53*(3), 752–771. https://doi.org/10.1175/JAMC-D-13-0126.1

Turner, D. D., & Löhnert, U. (2021). Ground-based temperature and humidity profiling: Combining active and passive remote sensors. *Atmospheric Measurement Techniques*, *14*(4), 3033–3048. https://doi.org/10.5194/amt-14-3033-2021

Turner, D. D., & Mlawer, E. J. (2010). Radiative heating in underexplored bands campaigns (RHUBC). *Bulletin America Meteorology Social*, *91*, 911–923. https://doi.org/10.1175/2010BAMS2904.1

Turner, D. D., Mlawer, E. J., & Revercomb, H. E. (2016). Water vapor observations in the ARM program. The Atmospheric Radiation Measurement Program: The First 20 Years. Meteor. Monograph. *Meteorological Monographs*, *57*, 13.1–13.18. https://doi.org/10.1175/AMSMONOGRAPHS-D-15-0025.1

Turner, D. D., Tobin, D. C., Clough, S. A., Brown, P. D., Ellingson, R. G., Mlawer, E. J., et al. (2004). The QME AERI LBLRTM: A closure experiment for downwelling high spectral resolution infrared radiance. *Journal of the Atmospheric Sciences*, *61*(22), 2657–2675. https://doi.org/10.1175/jas3300.1

Wang, J., Cole, H. L., Carlson, D. J., Miller, E. R., Beirle, K., Paukkunen, A., & Laine, T. K. (2002). Corrections of humidity measurement errors from the Vaisala RS80 radiosonde – Application to TOGA COARE data. *Journal of Atmospheric and Oceanic Technology*, *19*(7), 981–1002. https://doi.org/10.1175/1520-0426(2002)019<0981:cohmef>2.0.co;2

Wargan, K., Labow, G., Frith, S., Pawson, S., Livesey, N., & Partyka, G. (2017). Evaluation of the ozone fields in NASA's MERRA-2 reanalysis. *Journal of Climate*, *30*(8), 2961–2988. https://doi.org/10.1175/JCLI-D-16-0699.1

Westwater, E., Churnside, J., Shaw, J., Snider, J. B., Gage, K. S., Han, Y., et al. (1995). Ground-based remote sensor observations during the PROBE experiment in the tropical western Pacific. In *1995 international geoscience and remote sensing symposium, IGARSS'95. Quantitative remote sensing for science and applications* (Vol. 2, pp. 882–886). IEEE. https://doi.org/10.1109/IGARSS.1995.521086

Worden, H. M., Francis, G. L., Kulawik, S. S., Bowman, K. W., Cady-Pereira, K., Fu, D., et al. (2022). TROPESS/CrIS carbon monoxide profile validation with NOAA GML and ATom in situ aircraft observations. *Atmospheric Measurement Techniques*, *15*(18), 5383–5398. https://doi.org/10.5194/amt-15-5383-2022

Worden, H. M., Logan, J. A., Worden, J. R., Beer, R., Bowman, K., Clough, S. A., et al. (2007). Comparisons of Tropospheric Emission Spectrometer (TES) ozone profiles to ozonesondes: Methods and initial results. *Journal of Geophysical Research*, *112*(D3), D03309. https://doi.org/10.1029/2006JD007258